



HAL
open science

Heat transfer and flow velocity study of a row of jets emerging from a perforated pipe at a low Reynolds number

Yassine Ahmimache, Matthieu Fénol, Frédéric Plourde, Laurent Descamps

► **To cite this version:**

Yassine Ahmimache, Matthieu Fénol, Frédéric Plourde, Laurent Descamps. Heat transfer and flow velocity study of a row of jets emerging from a perforated pipe at a low Reynolds number. *International Journal of Heat and Mass Transfer*, 2022, 183, pp.122067. 10.1016/j.ijheatmasstransfer.2021.122067 . hal-03617210

HAL Id: hal-03617210

<https://hal.science/hal-03617210>

Submitted on 5 Jan 2024

HAL is a multi-disciplinary open access archive for the deposit and dissemination of scientific research documents, whether they are published or not. The documents may come from teaching and research institutions in France or abroad, or from public or private research centers.

L'archive ouverte pluridisciplinaire **HAL**, est destinée au dépôt et à la diffusion de documents scientifiques de niveau recherche, publiés ou non, émanant des établissements d'enseignement et de recherche français ou étrangers, des laboratoires publics ou privés.



Distributed under a Creative Commons Attribution - NonCommercial 4.0 International License

Title: Heat transfer and flow velocity study of a row of jets emerging from a perforated pipe at a low Reynolds number

Yassine Ahmimache^{1,2}, Matthieu Fénot¹, Frédéric Plourde¹, Laurent Descamps²

¹Institut Pprime, CNRS, ENSMA, Université de Poitiers, 1 Avenue Clément Ader, BP 40109, 86961 Futuroscope Chasseneuil Cedex, France

²Safran Aircraft Engines Villaroche, Rond Point René Ravaud - Réau, 77550 Moissy-Cramayel, France

Abstract

Aerodynamic and thermal experimental investigations were carried out on a row of circular low Reynolds jets emerging from a perforated pipe. Particle Image Velocimetry and Infrared Thermography were performed to determine flow velocity fields and local Nusselt number variations along the impinged plate. Jet Reynolds number ($1500 < Re_j < 5000$), upstream crossflow in the pipe ($1.5 < VR < 9.7$), injection-to-plate distance ($3 < H/d < 7$) as well as center-to-center jet spacing ($2.25 < p/d < 5.8$) were all taken into account. Measurements were compared to those of a fully developed circular jet issuing from a long tube under the same conditions ($3000 < Re_j < 5000$ and $3 < H/d < 7$). Experimental results showed that jets tend to emerge with an effective cross-sectional area reduced to a crescent shape unlike that of axisymmetric fully developed jets; their specific structure was attributed to flow deflection from the pipe to the holes and resulted in heat transfer specificities differing from those of a fully developed jet. Heat transfer rates were found to be primarily dependent on injection Reynolds number, injection-to-plate distance and center-to-center spacing, and they were found to be relatively low compared to a fully developed jet.

Keywords: Jet impingement cooling; Row of jets; Single jet; Crossflow; Heat transfer coefficient; Infrared thermography; PIV

Highlights

- Jet impingement from a row of holes perforated in a pipe is studied at low Reynolds.
- Local heat transfer is determined with Infrared Thermography technique.
- Flow structure is determined with Particle Imaging Velocimetry (PIV) technique.
- Effect of Reynolds, crossflow, nozzle-to-plate and pitch distances are investigated.

- A perforated pipe configuration is compared to a fully developed jet.

Nomenclature

A_j Cross-sectional area of the injection hole [m²]

C_d Discharge coefficient [-]

D Inner pipe diameter [m]

d Injection diameter [m]

H Injection-to-impinged plate distance [m]

h Convective heat transfer on the impinged side of the plate [W/m²/K]

L_x, L_y, L_z Test section dimension [m]

M_j Single jet mass flow rate = $M_{j,tot}/n$ [kg/s]

$M_{j,tot}$ Total impinging mass flow rate [kg/s]

M_{pipe} Pipe mass flow rate at the entrance of the test section [kg/s]

n Number of injection holes [-]

$Nu[x, y]$ Nusselt number = hd/λ_{air} [-]

$\overline{Nu}[y]$ Line averaged Nusselt number [-]

\overline{Nu}_{6d} Surface averaged Nusselt number [-]

Nu_0 Nusselt number at stagnation point [-]

p Center-to-center jet distance [m]

Re_j Reynolds number = $\rho V_j d/\mu$ [-]

T_1 Jet temperature [K]

T_2, T_3 Test section temperature [K]

T_{amb} Ambient temperature [K]

T_{ref} Reference temperature [K]

T_w Wall temperature [K]

u, v, w Mean Cartesian velocity components [m/s]

$u_{rms}, v_{rms}, w_{rms}$ Root mean square Cartesian velocity components [m/s]

\overline{V}_j Injection mean flow rate velocity [m/s]

\overline{V}_{pipe} Pipe mean flow rate velocity at the entrance of the test section [m/s]

VR Velocity Ratio = $\overline{V}_j/\overline{V}_{pipe}$ [-]

x, y, z Cartesian coordinates [m]

r Radial coordinate [m]

Greek symbols

λ_{air} Air thermal conductivity [W/m/K]

λ_p Plate thermal conductivity [W/m/K]

μ Air dynamic viscosity [Pa·s]

ρ Air density [kg/m³]

ε_p Impinged plate emissivity [-]

φ_{cond} Conductive heat flux on the rear side [W/m²]

$\varphi_{conv,r}$ Convective heat flux on the rear side [W/m²]

φ_{conv} Convective heat flux on the impinged side [W/m²]

φ_{elec} Electrical flux dissipated by Joule effect [W/m²]

$\varphi_{rad,f}$ Radiative heat flux on the impinged side [W/m²]

$\varphi_{rad,r}$ Radiative heat flux on the rear side [W/m²]

φ_{losses} Total heat flux losses [W/m²]

1. Introduction

Jet impingement effectively enhances convective heat transfer and is consequently widely used in various applications necessitating high heat transfer rates such as the cooling of electronics components and food product drying. Impinging jets are also widely used either to cool or to heat modern aero-engine components such as in turbine blade cooling, outer wall of turbine casing cooling, and anti-icing systems for wings.

Although widely studied, impinging jets remain a complicated phenomenon involving complex thermal interactions between fluid and wall as well as highly specific jet flow mechanisms. Several experimental and numerical overviews have been conducted ([1–4]). More specifically, the most widely studied configuration is a single jet issuing from a long tube or a contraction nozzle; impingement of this type of jet on a flat surface serves as a reference configuration.

The jet region in the vicinity of the injection nozzle, called free jet, has been defined as a potential core surrounded by a shear layer (Gauntner et al. [5]). The potential core is a low-lying turbulent region in which mean velocity remains constant. Previous studies on turbulent jets ([6,7]) have shown that turbulent intensity is generally inferior to 8%. Potential core length is commonly defined as the distance from the nozzle exit to the area where axial velocity has decreased to 95% of the initial axial velocity. In the review by Gauntner et al. [5], length of the potential core can be expressed in terms of injection diameter d , and has been found experimentally to range from approximately $4.7d$ to $7.7d$ depending on the nozzle configuration; the authors recommend using $6.1d$ for unknown value of the potential core. Contrarily to **the potential core region**, the shear layer is a high-lying turbulent region, where turbulent intensity approximates 20% ([6,7]). Studies have unequivocally shown that overall heat transfer depends strongly on the injection Reynolds number Re_j based on the injection diameter d and the impingement height H/d as well as a number of other parameters: nozzle shape, jet temperature, upstream air supply ([8–11]). The heat transfer coefficient has been shown to peak at the stagnation point, **with the magnitude depending on** depends on H/d . The optimal heat transfer coefficient has been reached for $H/d = 6$, which corresponds to the potential core length of the jet ([12,13]). For low injection-to-plate distances $H/d < 4$, radial distribution of the heat transfer coefficient presents a secondary peak (Baughn and Shimizu [14]). Its location ranges from $r/d = 1.2$ to $r/d = 2.1$, and intensity depends on both the Reynolds number and nozzle-to-plate distance. Maximum level

is commonly attributed to the interaction of shear layer vortexes with the impinged wall and to the formation of secondary vortexes ([15,16]).

Most of the quoted studies deal with heat transfer characteristics due to jet impingement for relatively high Reynolds numbers. McNaughton and Sinclair [17] defined such a jet - $Re_j > 3000$ - as fully turbulent. Complementary studies ([8,18–20]) have been devoted to jet impingement cooling for fully turbulent jets with low Reynolds numbers ($3600 < Re_j < 6400$), and the authors found no major heat transfer differences compared to jets with much higher Reynolds numbers. McNaughton and Sinclair [17] also classified the flow structure of free jets with lower Reynolds numbers ($1000 < Re_j < 3000$), which are known as semi-turbulent jets; up to a certain distance from a jet exit, there is no apparent entrainment of the surrounding fluid. Kuang et al. [21] presented a comprehensive investigation of round impinging jets for semi-turbulent flow ($1800 < Re_j < 2800$). As pointed out by McNaughton and Sinclair [17], Kuang et al. [21] showed that the free jet region of semi-turbulent jets is essentially an undisturbed flow region consisting of laminar length and followed by the potential turbulent core. When the impinged plate is located inside the undisturbed region, overall heat transfer remains almost unchanged, whereas when the plate is located outside this region, optimal heat transfer is achieved at the end of the potential core. Katti et al. [9] compared transitional effects on heat transfer for Reynolds numbers ranging from 500 to 12000 and jet-to-plate spacing from $0.5d$ to $8d$. With low jet-to-plate spacing, while they observed a classical secondary peak for $Re_j = 12000$, for lower Reynolds number values they found only an inflection point, and a continuously decreasing curve of Nusselt number distribution below $Re_j = 3000$. **A study performed by Rohlfs et al. [22] offers further explanations regarding the cause of second peaks in the radial distribution of Nusselt number at low injection Reynolds.** Lastly, McNaughton and Sinclair [17] classified free jet flow structure with $300 < Re_j < 1000$ as fully laminar jets; in their model, there is no obvious perturbation from the surrounding fluid through the whole jet field. From here on, our literature review will focus mainly on low Reynolds numbers.

Previously described circular single injection serves as a reference configuration. However, single jet impingement produces non-uniform heat transfer, which is not at all conducive to surface cooling. Consequently, multi-jet impingement is extensively used in industrial cooling. Rows of impinging jets bring into play a number of additional parameters such as distance between injection holes and jet interactions before and after injection. Viskanta [1] provided a general overview of the key experimental studies devoted to multi-jet

impingement. Carcasci [23] applied a smoke visualization technique to study the flow of a row of air jets, and found an interaction area midway between the stagnation zone boundaries; that is where the vortexes and adverse vortexes are visible at the meeting points of the jets. This phenomenon, which results from the wall jet interactions, is known as the fountain effect.

Wright et al. [24] focused on heat transfer and reviewed correlation for a row and an array of circular jets impinging over a flat surface. Several other teams [25–27] carried out experiments aimed at determining the heat transfer characteristics due to a single inline row of jets. Geometric parameters such as nozzle exit-to-flat surface spacing, spacing between two adjacent nozzles and jet Reynolds number were investigated. Fénot et al. [26] showed that in high jet center-to-center spacing (from $p/d > 4$), local Nusselt number distributions near the stagnation point are approximately identical to those of a single jet. As for smaller jet center-to-center spacing ($p/d < 4$), the influence of adjacent jets seems to be limited in the region where the jets meet. Maximum heat exchange midway between jets has been demonstrated by many authors [12,26–28], especially for small injection-to-plate spacing and jet-to-jet spacing, and is commonly attributed to the fountain effect.

Studies on the configuration of inline rows have been complemented by other interesting and relevant works [1,29,30]. For example, Viskanta [1] showed that a significant difference with single circular jet is the optimum injection-to-plate distance leading to maximum heat transfer. While the latter was achieved in a single impinging jet at the end of the potential core (about 6 diameters downstream), the researchers [1] observed that maximum heat transfer from arrays of jets occurs about 1-2 diameters downstream with $p/d > 0.5$. Huber and Viskanta [29] and Hollworth and Berry [30] found that adjacent jet interference before impingement becomes limited when p/d is higher than 8, in which case Nusselt numbers for an array of jets and a single jet become similar.

A large number of studies have dealt with the influence of injection nozzle shape, with jets issuing from a long tube, a convergent nozzle or an orifice. In these different works, air supply before the injection runs in the same axis nozzle direction. On the other hand, jets emerging from an air supply orthogonal to the injection nozzle axis have been sparsely studied and are far from being completely understood. Impinging jets issuing from such configurations are yet widely used, particularly in aero-engine components such as anti-icing systems for wings by means of piccolo tube (Pachpute and Premachandran [31]) or cooling of

casing for the outer wall of the turbine by means of active clearance tube (Da Soghe et al. [32]).

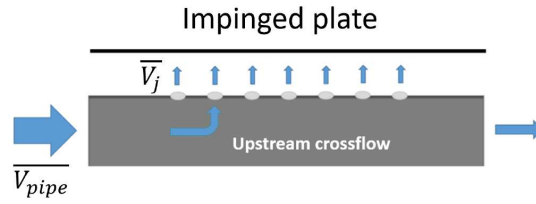


Fig. 1: Perforated pipe configuration

For such a configuration (Fig. 1) and unlike classical rows of jets, the mass flow rate split across the tube is not homogeneous. It bears mentioning that accurate evaluation of the impinging jet mass flow rate and the associated heat transfer coefficient is fundamental. With this in mind, some researchers (Da Soghe et al. [32] and Hay and Lampard [33]) have attempted to characterize the discharge coefficient C_d across the injection holes, which is defined as the ratio of the actual mass flow rate through a hole and the isentropic flow rate. A C_d correlation was established by Da Soghe et al. [32], who also showed that the mass flow rate split across the tube can be highly variable. The same experimenters [34] pointed out that the mass velocity ratio between the jet and the flow in the pipe, $(\rho \bar{V})_j / (\rho \bar{V})_{pipe}$ is a key parameter. They observed that geometries for which this ratio is greater than 5 lead to constant impingement jet mass flow rate distribution, whereas pronounced differences in jet mass flow rate distribution have been observed for geometries characterized by a low mass velocity ratio.

Focusing on the thermal aspect, some authors have attempted to characterize heat transfer ([31,35,36]) and demonstrated that compared to jets issuing from a long tube (or convergent nozzle), local heat transfer rates are lower. However, the respective influences of common heat transfer parameters such as jet-to-plate distance, center jet pitch and the upstream flow in the tube have yet to be conclusively determined. Regarding the flow structure of jets, the main works ([31,36,37]) have been limited to a numerical RANS approach. Pachpute and Premachandran [31] observed dissimilarities between injection exit velocity distributions along the rows of jets. On the one hand, the first jets are strongly influenced by upstream air supply; they emerge from the injection holes with a deflection angle, resulting in non-perpendicular flow to the impinged plate. On the other hand, the last jets impinge normally to the impinged surface and are only minimally deflected. These numerical studies show that heat transfer and flow structure in jets with this type of configuration are very different from jets issuing from a single circular injection, as was

experimentally confirmed by Fénot and Dorignac [38], who studied a jet issuing from a rectangular pipe. They showed that due to upstream flow influence, injection flow is not axisymmetric, and that the flow in the injection zone has a crescent shape. Regarding heat transfer, they observed lower Nusselt numbers than in single circular jets. The influence of five different parameters (Reynolds number, upstream and downstream crossflow, injection-to-plate distance, thickness of the injection hole) was likewise taken into account, and they reported that the most important parameters are the injection Reynolds number and injection-to-plate spacing.

Article	Configuration	Reynolds and geometric parameters	Measurements
Katti et al. [9]	Single jet	$500 < Re_j < 8000$ $0.5 < H/d < 8$	Nusselt
McNaughton and Sinclair [17]	Single jet	$100 < Re_j < 28000$ Free jet	Flow visualization
Kuang et al. [21]	Single jet	$1800 < Re_j < 15000$ $3 < H/d < 33$	Flow visualization Nusselt
Wright [24]	Row of jets	$2000 < Re_j < 124000$ $1 < H/d < 58 ; 2 < p/d < 30$	Review of Nusselt correlations
Goldstein and Seol [25]	Row of jets	$2000 < Re_j < 124000$ $2 < H/d < 8 ; 4 < p/d < 8$	Nusselt
Fénot et al. [26]	Row of jets	$Re_j = 23000$ $2 < H/d < 5 ; 4 < p/d < 8$	Nusselt
Fénot and Dorignac [38]	Single jet with upstream crossflow	$5000 < Re_j < 23000$ $2 < H/d < 10$	Nusselt Velocity fields
Soleimani Nia et al. [39]	Single jet with upstream crossflow	$16500 < Re_j < 19500$ Free jet	Velocity fields
Da Soghe et al. [34]	Row of jets with upstream crossflow	$1.05 < P_{inlet,pipe}/P_{out} < 1.15$ $H/d = 7 ; 1.5 < p/d < 12$	Nusselt Pressure drop
Pachpute and Premachandran [31]	Row of jets with upstream crossflow	$5000 < Re_j < 20000$ $2 < H/d < 12 ; 1.4 < p/d < 2.9$	Nusselt

Table 1: Impingement cooling studies for single and row of jets

Based on these different articles (summarized in Table 1), it appears that only a few studies have been carried out on upstream crossflow configurations (Fig. 1), mainly with relatively high injection Reynolds numbers ($Re_j > 5000$). To our knowledge, velocity measurement and experimental flow structure characterization on impinging jets have yet to be achieved. To fill the gap, we performed both aerodynamic and thermal experimental investigations on a single line of seven jets emerging from a pipe and impinging on a plate at a low Reynolds number. The influencing tested parameters are the injection Reynolds number Re_j , the upstream crossflow quantified through a velocity ratio VR between the jet and the

flow entering the pipe, the injection hole to plate spacing H/d and the center-to-center injection hole spacing p/d . The jet flow structure and resulting heat transfer of such configurations were also compared to a fully developed jet issuing from a circular injection for the same ranges of Re_j and H/d .

2. Facilities and methods

2.1. Experimental Setup

As presented in Fig. 2, the apparatus has been designed with the aim of independently varying each geometric and aerodynamic influencing the parameters. It consists of an air supply system, a long tube that ensures a fully developed inlet flow and a test section where jets emerging from the perforated pipe impinge a plate. Pipe and test section exits allow mass flow rate regulation through both the pipe and the injection holes.

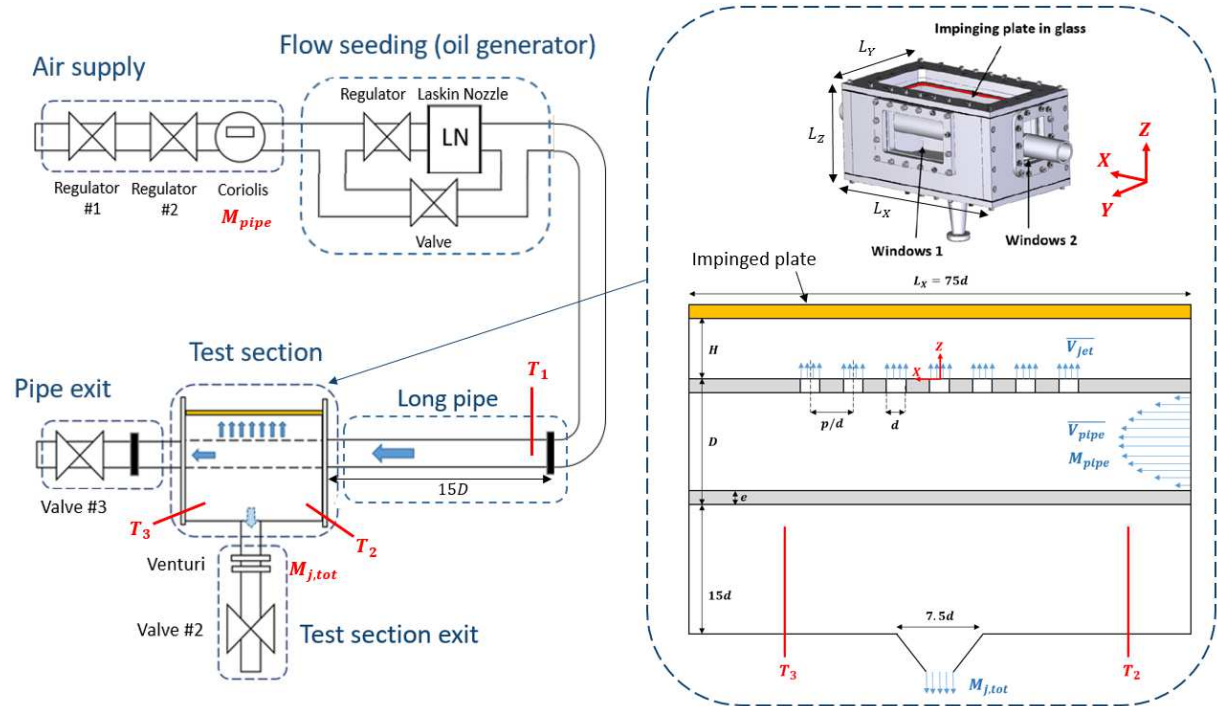


Fig. 2: Schematic view of the experimental setup

Continuous airflow entering the pipe is supplied by the laboratory pressure-air circuit. As laboratory supply pressure can vary slightly, two regulators installed in series providing a two-stage pressure drop are used to adjust the upstream pressure with high sensitivity. A Coriolis flowmeter (Emerson CMFS015) measures the mass flow rate with 0.25% uncertainty and 0.20% repeatability, as well as the temperature with 1°C uncertainty and 0.2°C repeatability. For velocity measurements, an oil generator combined with a

regulator is placed in front of the long pipe to generate tracer particles in the airflow. The oil generator system is turned off for heat measurements, and airflow goes through a bypass. A long pipe is then connected to the air supply with a junction located $15D$ from the extremity of the testing section to ensure that the flow is fully developed when it nears the injection holes. At the end of the pipe, the junction is placed $4D$ from the extremity of the testing section to avoid any perturbation due to a connector in the vicinity of the injection holes. At the extremity of the pipe, a valve controls mass flow rate through the pipe. In order to separately control the mass flow rate in the pipe and through the injection holes, the impingement is confined to a test section. The impinging jet flow then exits the test section from the bottom side through a converging section, and a valve is placed downstream to control the total mass flow rate impinging the plate. A venturimeter is positioned **downstream** the converging section to measure the mass flow rate **leaving the test section** $M_{j,tot}$. **The venturimeter and associated pressure converters have previously been calibrated between 0.2g/s and 2.1g/s to cover the mass flow rate range used in the experiment (less than 2 % uncertainty on $M_{j,tot}$). Flow distribution through the seven injection holes is considered uniform; this assumption will be discussed in section 3.1. The mass outflow rate of one hole, M_j , is obtained by dividing the total mass flow rate leaving the test section, $M_{j,tot}$, by the number of holes.** The injection Reynolds number, Re_j , is hence defined in terms of the average mass flow rate per hole:

$$Re_j = \frac{M_{j,tot}d}{nA_j\mu} \quad (1)$$

with $M_{j,tot}$, the total mass flow rate leaving the test section, A_j , the cross-sectional area of a circular hole, n , the number of holes. **The jet and pipe mean flow rate velocities, $\overline{V_{jet}}$ and $\overline{V_{pipe}}$, are deduced from injection mass flow rate, M_j , and inlet mass flow rate M_{pipe} .** The velocity ratio, $VR = \overline{V_{jet}}/\overline{V_{pipe}}$, is then controlled by independently varying the mass flow rate through the pipe and the injection holes.

One thermocouple, T_1 , is located in the entry of the pipe and indicates the temperature of the jet. Two thermocouples, T_2 and T_3 , in the test section specify the ambient temperature inside. Two thermocouples in the room give the ambient temperature. **Temperatures are measured with type K thermocouples (0.7K relative accuracy).**

2.2. Geometric and aerodynamic conditions

For all measurements, perforated pipes present a line of seven holes. The hole diameter d is fixed, the outer pipe diameter was set at $D = 10d$ and pipe thickness at $e = 0.9d$. Tested aerodynamic parameters are the injection Reynolds number Re_j , the upstream crossflow VR , tested geometric parameters are the injection hole to plate spacing H/d and the center-to-center injection hole spacing p/d (Table 2).”

Parameters	Values [-]					
	Perforated pipe configuration			Fully developed jet		
Re_j	1500	3000	5000	3000	5000	
VR	1.5	2	4	9.7	/	
H/d	3	5	7	3	5	7
p/d	2.25	3.5	5.8	/		

Table 2: Aerodynamic and geometric tested conditions

The test section measures $L_x = 75d$ long by $L_y = 40d$ wide and $L_z = 28d$ high for the smallest injection-to-plate distance (Fig. 2). It was designed so as to be large enough to limit confinement and reduce edge effects; minimum distance between the holes and the edge of the test section is $20d$. The spanwise direction along the injection hole is defined by X-axis, the streamwise direction by Y-axis, and the axial axis of the central hole by Z-axis. Two windows in glass are installed (Fig. 2): Window 1 is located on the lateral side and allows direct visual access to the impinging jets in the plan (XZ). Window 2 includes a circular aperture with a diameter equal to the outer diameter of the pipe. This window allow direct visual access to the impinging jets in the plan (YZ). The impinged plate is located at a distance H/d from the injection hole and positioned orthogonally to the jet axis. Injection-to-plate distance is adjustable by means of spacers of various thickness. **Two impinged plate are used as target surface: a glass plate for velocity measurements and a heating plate for heat transfer measurements.**

Experiments carried out for jets emerging from a perforated pipe configuration were also compared to a fully developed jet issuing from a long tube ($28d$ length). Aerodynamic and geometric tested parameters are reported in Table 2.

2.3. Velocity measurement

Flow dynamics is characterized by planar Particle Image Velocimetry (PIV) technique, which is based on the measurement of instantaneous 2D-velocity fields. To characterize the potential 3D effects of the flow, the PIV measurement is carried out for six different planes (Fig. 3):

- Three (XZ) planes for $y/d = -0.25, 0$ and 0.25
- Three (YZ) planes for $x/d = -0.25, 0$ and 0.25

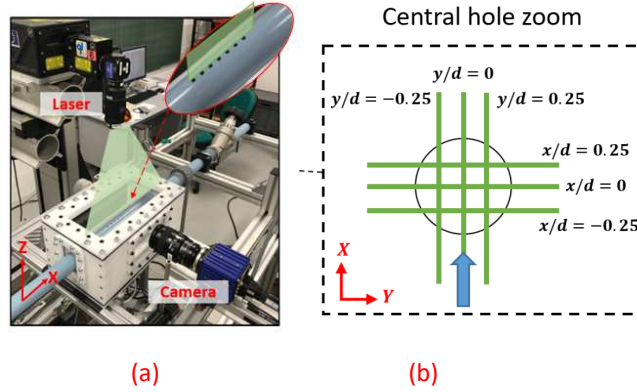


Fig. 3: PIV setup (a) 3D view, (b) location of six measurement planes

The flow is seeded by means of a Laskin Nozzle generating small oil particles in front of the tube, with average particle diameter at approximately $2\mu\text{m}$. The particles are then illuminated by a thin laser light sheet passing through the impinged glass plate. The ratio of the hole injection diameter d over the laser plane thickness is between 8 and 10, thereby avoiding potential 3D effect error due to the averaging of the jet's speed components over the width of the laser light sheet. The light intensity scattered by the tracer particles is recorded with a 25Hz frame rate camera ($2560 \times 2160 \text{ px}^2$) over a 15s time span. The delay between two laser pulses is between $9\mu\text{s}$ and $120\mu\text{s}$ depending on aerodynamic conditions. 375 images are recorded to obtain time averaged velocity components (u, v, w). The root mean square velocity components ($u_{rms}, v_{rms}, w_{rms}$) are equal to the standard deviation and refers to fluctuating velocity components.

Velocities were estimated using LaVision's DaVis 8.4 software. To enhance particle contrast intensity and reduce background noise, a black background is placed behind the laser light sheet and background image subtraction takes place. Cross-correlation is applied: from an initial pass 64×64 to 32×32 with 50% overlap. Spatial resolution is equal to $0.039d \times 0.039d$ for (XZ) planes and $0.082d \times 0.082d$ for (YZ) planes.

The uncertainties of PIV measurements are relatively hard to calculate accurately due to the numerous biases to be taken into account and because some of them cannot easily be quantified: out-of-plane-motion, scale calibration, seeding density, etc. Recently, PIV uncertainty quantification has been a focus of study (Neal et al. [40] and Sciacchitano et al. [41]). Wieneke [42] attempted to calculate an uncertainty value for individual instantaneous velocity vectors. Sciacchitano and Wieneke [43] also studied uncertainties for derived quantities such as vorticity and Reynolds stress. Uncertainty of the time-averaged quantities was found to be accurate within 5%, whereas that of RMS quantities is accurate within 10%.

2.4. Heat transfer measurement

The local heat transfer coefficient on the impinged plate is calculated using infrared thermography and the heated foil technique. The target surface is a 0.8mm thick epoxy plate covered with a thin foil of copper (17.5 μ m thick) engraved to form a circuit linked to a DC supply and to allow heating of the plate by Joule effect. **The plate is painted in black in both sides to obtain high uniform emissivity ($\epsilon = 0.95 \pm 0.02$) for precise radiative heat flux calculation and thermographic measurements.** Thermographic measurement on the back side of the plate is achieved using an infrared camera (FLIR X6580sc) with 17mK thermal sensitivity at 300K. The 0.8mm thin impinged plate ensures that the Biot number is low enough (inferior or close to 0.1) to assume that wall temperature on both faces of the impinged plate is the same when thermal equilibrium is reached. The heating circuit is engraved solely in the center of the impinged plate to reduce the heating zone (rectangle 15 d wide by 20 d long in Fig. 4). Consequently, the maximal difference between plate and jet temperature is inferior to 60°C and the Richardson number value is low enough to neglect natural convection effect.

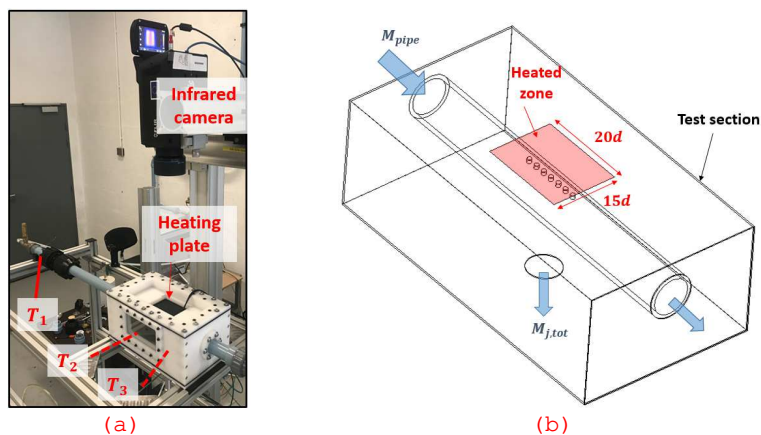


Fig. 4: Infrared camera setup (a) 3D view (b) schematic view of the test section

The method has been described in previous papers [44,45]. The principle is based on the definition of the heat transfer coefficient characterized by Newton's law:

$$T_w = \frac{\varphi_{conv}}{h} + T_{ref} \quad (2)$$

with φ_{conv} , convective heat flux density on the impinged side, T_w , the temperature of the wall on the same side and T_{ref} , the reference temperature of the fluid. For a given aerothermal configuration, at a specific position on the wall, the method consists of imposing four different convective heat flux densities φ_{conv}^i ($i = 1, \dots, 4$) and recording the backside temperature T_w^i . Considering equation (2) and assuming that the heat transfer coefficient h and the reference temperature T_{ref} are independent of flux density and wall temperature at a specific position on the wall, a linear trend line is drawn locally through the four couples $(\varphi_{conv}^i, T_w^i)$. As seen in equation (2) and 5, the linear regression slope corresponds to $1/h$, while the extrapolated $\varphi_{conv} = 0$ abscissa indicates the reference temperature T_{ref} .

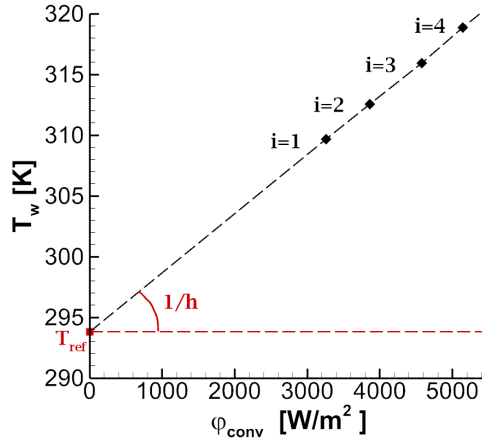


Fig. 5: Linear regression method

In practice, the impinged plate is heated by imposing electrical intensity in the copper circuit. The electrical flux density dissipated by Joule effect, $\varphi_{elec}(x, y)$, is then calculated locally taking into account the variation of electrical resistivity with temperature. After impinged plate thermal equilibrium is achieved, the temperature is recorded on the back side of the plate using an infrared camera. Temperature cartography, $T_w(x, y)$, is the average of 375 thermographic images registered over 15s and 25Hz frame rate so as to reduce measurement noises. A local heat balance for each grid point, defined as one pixel of the cartography temperature, is then achieved in order to determine the convective heat flux density exchange between the impinged plate and the jet $\varphi_{conv}(x, y)$:

$$\begin{cases} \varphi_{conv} = \varphi_{elec} - \varphi_{losses} \\ \varphi_{losses} = \varphi_{rad,r} + \varphi_{rad,f} + \varphi_{conv,r} + \varphi_{cond} \end{cases} \quad (3)$$

Radiative losses on front side, $\varphi_{rad,f}$ and on rear side, $\varphi_{rad,r}$ are calculated through Stefan Boltzman's law. The convective losses on the rear side, $\varphi_{conv,r}(x,y)$ are then calculated from a heat transfer coefficient on rear side equal to $6\text{W/m}^2/\text{K}$. To determine this value, an experiment is conducted by heating the front side of the plate without any impinging jets and by recording the backside temperature, and insulation is placed tight against the front side surface of the impinged plate. It results in $\varphi_{elec} = \varphi_{losses}$ in Equation 3, the heat transfer coefficient on the rear side is hence obtained by resolving the heat balance. The conductive heat flux density exchanged sideways between adjacent grid points, $\varphi_{cond}(x,y)$, is also considered through Fourier's law. The number of grid points is high enough to capture heat conduction (minimum spatial resolution of $7.3\text{px}/d$). Typical values of the total heat flux losses, φ_{losses} , represents about 15% of the electrical flux dissipated by Joule effect, φ_{elec} . By repeating this procedure four times with different electrical flux densities φ_{elec}^i , the cartographies of local convective heat transfer coefficient h and fluid reference temperature T_{ref} are deduced. Hence, for each pixel of the front side of the plate, the Nusselt number is defined as:

$$Nu[x,y] = hd/\lambda_{air}$$

where λ_{air} is the air thermal conductivity.

As presented in Fig. 5, determining the uncertainty of the heat transfer coefficient h requires first to estimate the uncertainties of both convective heat flux φ_{conv}^i and wall temperature T_w^i . The uncertainty of the infrared camera is noted above while the uncertainty of φ_{conv}^i is obtained with a statistical approach using error propagation in Equation 3. The uncertainty values have been reported at a 95% confidence level. The uncertainty of the heat transfer coefficient h is then determined using a Monte Carlo approach [46]. It consists of repeating random sampling for φ_{conv}^i and T_w^i to calculate h for these specific parameter values. Sample parameters of φ_{conv}^i and T_w^i have been chosen from a Gaussian distribution. Overall uncertainty values for the Nusselt number are then deduced and are estimated between 6% and 12%. The region of maximum error is found in the center line zone, between stagnation points. Relative uncertainty values between the measurements are estimated to be under 5%.

2.5. Validation study

The measurement method regarding the Infrared Thermography technique has been validated in previous works conducted by the authors [47]: local Nusselt distributions resulting from a fully developed axisymmetric jet emerging from a long tube are compared with results from prior published papers (Baughn and Shimizu [14], and Lee et al.[48]). Comparison at $Re_j = 23000$ and $H/d = 2$ shows good agreement (less than 12 %).

Keeping in mind that the present work focuses on jet impingement at low Reynolds numbers, the validation study was completed with additional experiments performed within our study range ($3000 < Re_j < 5000$). Due to lack of published literature at low Reynolds number, radial Nusselt distributions obtained in published studies are reported for several injection-to-plate distances in Fig. 6 (a) and (b). These results are consistent with experiments performed in this present study.

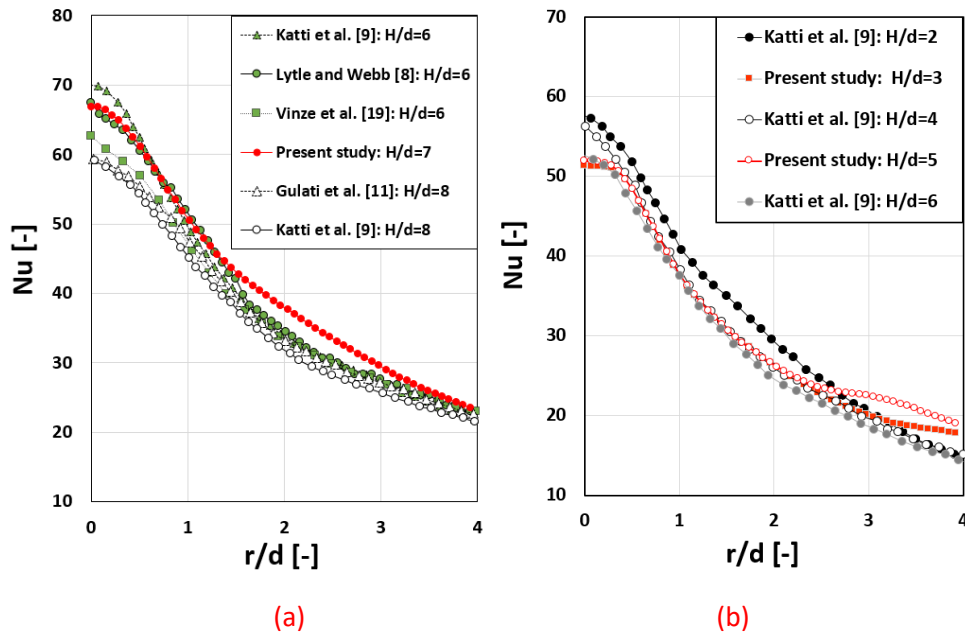


Fig. 6: Present study and literature comparison: (a) $Re_j = 5000$, (b) $Re_j = 3000$

3. Results

3.1. Jet flow structure

In this section, the overview flow structure of jets emerging from a perforated pipe (Fig. 1) is described and then compared to a reference configuration corresponding to a single fully developed jet issuing from a long tube at the same injection Reynolds and injection-to-plate distance. As global jet flow structure for a perforated pipe geometry remains similar for

all tested cases, results are presented for a specific configuration ($Re_j = 5000$, $VR = 2$, $H/d = 7$ and $p/d = 3.5$). The described conditions illustrate the complete development of jets ($H/d = 7$) and highlight the effect of upstream crossflow within the pipe ($VR = 2$). Specific features visible for other tested cases will be reported below, particularly in regards to the influence of injection Reynolds number, upstream crossflow and injection-to-plate distance.

Fig. 7 (a) and (b) present a close-up look of velocity profiles near the injection holes of the perforated pipe in the plane $y/d = 0$. Mean and RMS velocity profiles of the three central jets are reported along $z/d = 0.1$. As seen in Fig. 7 (a), a region of high normalized velocity values is located between $x/d = 0.1$ and $x/d = 0.5$: in this region, normalized mean velocity is constant and equal to a maximum value, $w/\overline{V}_{jet} = 1.5$. In the upstream half (between $x/d = -0.5$ to $x/d = -0.1$), mean velocity values are equal or inferior to zero. It shows that jets issuing from the holes of the perforated pipe are not axisymmetric and tend to emerge only from the downstream half of the holes. These trends are also observed for the previous and the subsequent injection holes of which the centers are located at $x/d = -3.5$ and $x/d = 3.5$. It can be deduced that jets emerge from a cross-sectional area of reduced size in comparison to the total hole area. More precisely, as the flow across the perforated holes is fed perpendicularly, it results in a sudden 90° flow deflection from the pipe to the holes. Flow separation is likely to occur slightly after the upstream edge of the hole and leads to a cross-sectional area limited to the second half of the injection holes and to pronounced asymmetry. Mean velocity of a fully developed jet is also reported for the same Re_j and H/d in Fig 7 (a). Mean velocity profile along the line $z/d = 0.1$ is parabolic with a maximum value, $w/\overline{V}_{jet} = 1.2$, at $r/d = 0$. By contrast, a fully developed jet issuing from a long tube is axisymmetric and emerges from the total area of the hole, resulting in a lower value of maximum mean velocity. Studies carried out at much higher injection Reynolds numbers tend to confirm the same mean velocity distribution for jets issuing from a long tube: Fénot and Dorignac [38] reported maximum normalized mean velocity equal to 1.2 for turbulent injection Reynolds number $Re_j = 23000$.

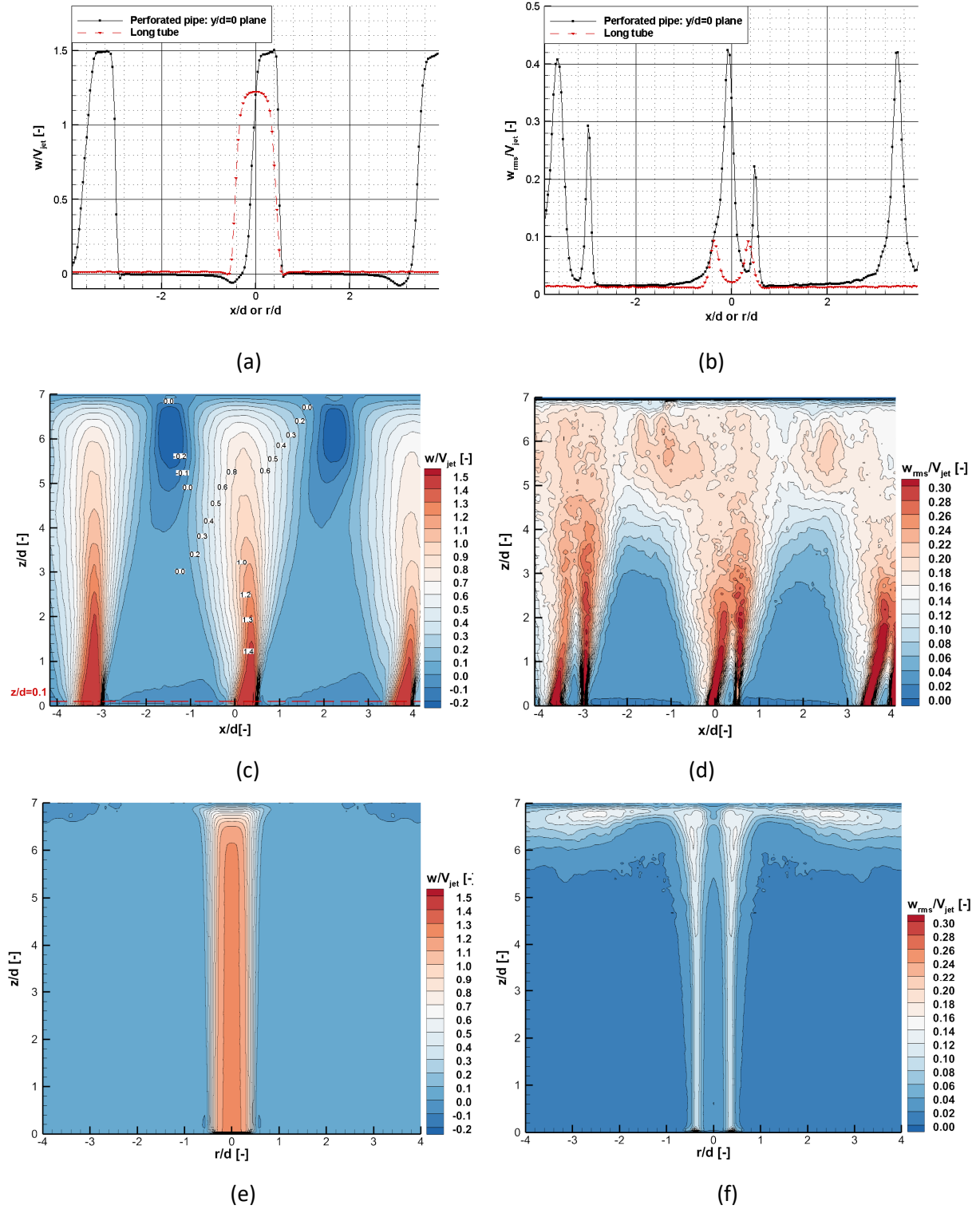


Fig. 7: Comparison of mean and RMS velocity distributions for perforated pipe configuration ($Re_j = 5000 - H/d = 7 - VR = 2 - p/d = 3.5$) and long tube configuration ($Re_j = 5000 - H/d = 7$). (a), (b): Velocity profiles along $z/d = 0.1$ - (c), (d): Perforated pipe: velocity field in $y/d = 0$ plane - (e), (f): Long tube: velocity field

Fig. 7 (b) presents RMS velocity along the line $z/d = 0.1$ for the three central jets: the region of maximum mean velocity described above is associated with low turbulence intensity, $w_{rms}/\overline{V_{jet}} < 5\%$. The zone is identified as the potential core and is surrounded by

high RMS velocity caused by the formation of vortex structures in the shear layer. Two dissymmetrical peaks of RMS velocity at $x/d = -0.05$ and $x/d = 0.5$ are visible with RMS velocity up to 40% and 23%. The shear layer in the downstream half ($x/d = 0.5$) is triggered by the lip of the hole. In contrast, near the upstream edge of the potential core, shear layer development is not initiated by the lip of the perforated hole since peak RMS velocity is located at $x/d = -0.05$ rather than $x/d = -0.5$. Gradient velocity between the jet (region with maximum mean velocity value, $1.5\overline{V}_{jet}$) and surrounding air sucked into the injection hole (region with negative mean velocity value) is particularly high and may trigger shear layer development. This gradient is larger than gradient velocity between the jet ($1.5\overline{V}_{jet}$) and the ambient air (zero velocity values) at the downstream edge of the hole. This is likely to result in higher turbulence intensity and may explain the higher peak in the shear layer located at the upstream edge of the potential core ($w_{rms}/\overline{V}_{jet} = 40\%$) compared to the downstream edge ($w_{rms}/\overline{V}_{jet} = 23\%$). A second explanation may be that the 3D aspect of the jet is much more pronounced in the upstream than in the downstream side of the jet. RMS velocity of a fully developed jet is also reported for the same Re_j and H/d in Fig 7 (b). Symmetrical peaks of RMS velocity are visible at $r/d = \pm 0.5$ and equal to 10%. Turbulent intensity in the shear layer of a fully developed jet issuing from a long tube is lower than the turbulence intensity of jets emerging from a perforated pipe. In regards to the jets emerging from perforated holes, their deflection from the main flow in the pipe and a higher velocity gradient between the jet and ambient air presumably generate more turbulence than the fully developed turbulent jet.

To conclude the discussion on the exit injection velocity profiles of a perforated pipe, more details about the dissymmetrical cross-sectional shape can be deduced from Fig. 8, which displays mean velocity field for three different planes in the streamwise direction. Only half planes are presented since velocity fields are symmetrical about plane $y/d = 0$. Close to the central exit hole (from $z/d = 0$ to $z/d = 1.5$), maximum mean velocity, $w/\overline{V}_{jet} = 1.5$, is observed in the plane $x/d = 0.25$. The same maximum mean velocity appears in the plane $x/d = 0$, but only at the edge of the hole. In contrast, close to the hole exit mean velocity is low or even negative in the middle of the hole and in the plane $x/d = -0.25$. One may deduce that the jet emerges only from the edge and in the second half of the hole. The effective cross-sectional area is then reduced to a crescent shape with larger width along Y-axis than X-axis. Considering the velocity profiles obtained along $z/d = 0.1$ for the six planes detailed in Fig. 3, the effective cross-sectional area is estimated to be between 60%

and 70% of the total hole area. Research by F enot and Dorignac [38] on a single jet issuing from a rectangular pipe at $Re_j = 23000$ confirms that injection flow tends to emerge from the injection hole with a prominent crescent shape, which persists until $z/d = 3$. This is particularly visible in the two planes $x/d = -0.25$ and $x/d = 0$ (Fig. 8 (a) and (b)), where the region of higher normalized mean velocity is not located close to the injection but far from the exit hole at approximately $z/d = 3$.

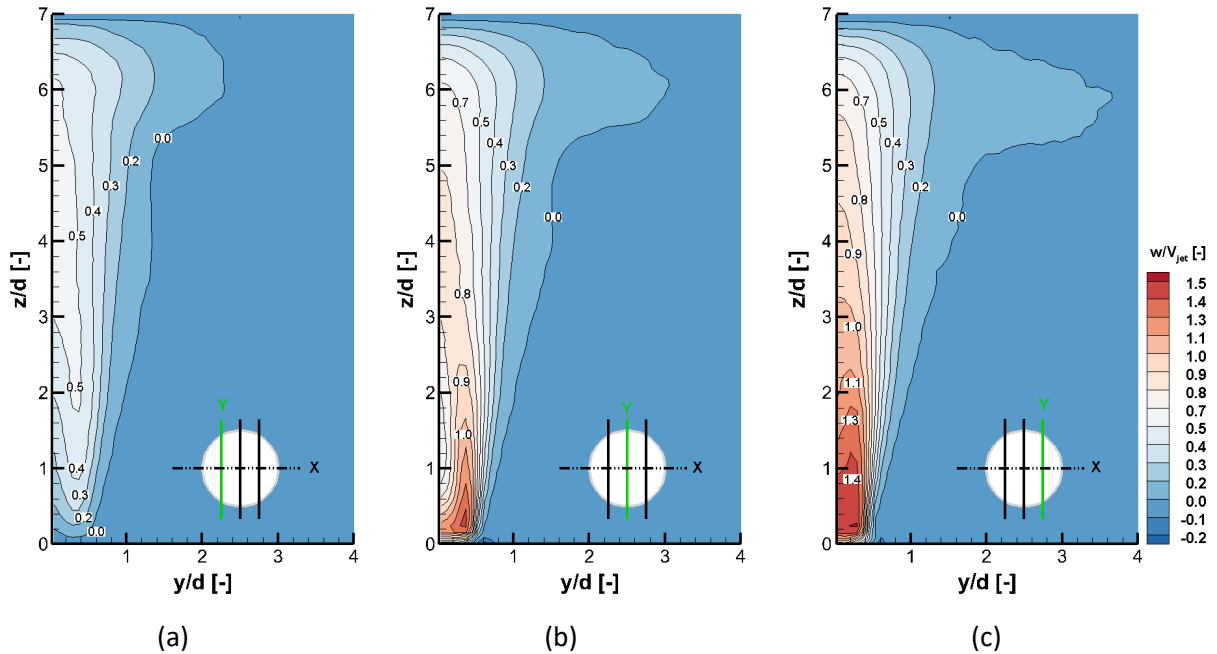


Fig. 8: Mean velocity fields in streamwise direction of the central jet: $Re_j = 5000 - H/d = 7 - VR = 2 - p/d = 3.5$. (a) Plane $x/d = -0.25$, (b) Plane $x/d = 0$, (c) Plane $x/d = 0.25$

Fig. 7 (c) and (d) presents the mean and RMS velocity fields of jets emerging from a perforated pipe in the plane $y/d=0$. The potential core, based on the distance from the hole exit to the location where mean velocity remains over 95% of the initial velocity, has been estimated at $1.4d$ for the central hole (Fig. 7 (c)). This is also noticeable in Fig. 7 (d): shear layers merge at approximately $z/d = 2.5$, slightly after the end of the potential core. By contrast, mean and RMS velocity fields of a fully developed jet are reported in Fig.7 (e) and (f): the maximum mean velocity is maintained at $6d$ downstream of the injection, and shear layers surrounding the potential core are still distinct at $z/d = 6$. The potential core of jets emerging from a perforated pipe is clearly smaller than the core corresponding to a fully turbulent jet issuing from a long tube. The difference in length of the potential core can be explained by various factors. First, jets issuing from a perforated pipe emerge only from the second downstream half of the holes, leading to a potential core at least half as thick as a core issuing from a long tube. Second, the crescent shape results in a higher perimeter-to-surface

ratio; shear layer development covers more space, leading to more rapid decrease of the mean velocity in the potential core. Finally, the reduced length of the potential core is also due to quicker growth of the shear layer than in a fully developed jet, as described further below.

Fig. 9 (a) illustrates a marked decrease of the mean velocity in the jet when it moves toward the plate: maximum normalized mean velocity is equal to $w/\overline{V}_{jet} = 1.3$ at $z/d = 2$ and falls to 0.9 at $z/d = 5$, while maximum mean velocity for the long tube configuration (Fig. 9 (c)) does not change between the hole exit and $z/d = 5$ ($w/\overline{V}_{jet} = 1.2$). The significant drop in mean velocity, **visible only for the perforated pipe configuration, can be first explained looking at the surrounding shear layer development. This growth is dyssymmetrical with a strong 3D aspect (Fig. 9 (b)).** On one side, downstream RMS peak intensity increases from 23% at $z/d = 0.1$ up to 30% at $z/d = 2$ and becomes larger due to the development of vortices in the shear layer. The nature of this enlargement is to some extent comparable to the growth of the shear layer of a **fully developed jet** (Fig. 9 (c)). On the other side, however, upstream shear layer growth is quite different; turbulent intensity decreases from 40% at $z/d = 0.1$ to 29% at $z/d = 2$ (Fig. 9 (b)); the decrease is probably due to the reduction of the 3D aspect of the jet as it grows away from the injection. The position of the peaks also tends to shift towards positive x value: from $x/d = -0.05$ at $z/d = 0.1$ to $x/d = 0.1$ at $z/d = 2$. This is most likely explained by emergence of the jets in the direction of the initial flow in the pipe. Downstream and upstream shear layers for the perforated pipe configuration grow by approximately 80% between $z/d = 0.1$ and $z/d = 1$ whereas there is no noticeable change for the long tube configuration. Consequently, **for jets emerging from a perforated pipe, higher turbulence intensity and the distinctive nature of the shear layer in each side of the jets might contribute to a quicker growth of the shear layer over the potential core and a drop in mean velocity. A significant dissymmetry in the free jet region resulting in the jet spreading in the perpendicular direction can also contribute to that velocity decrease.**

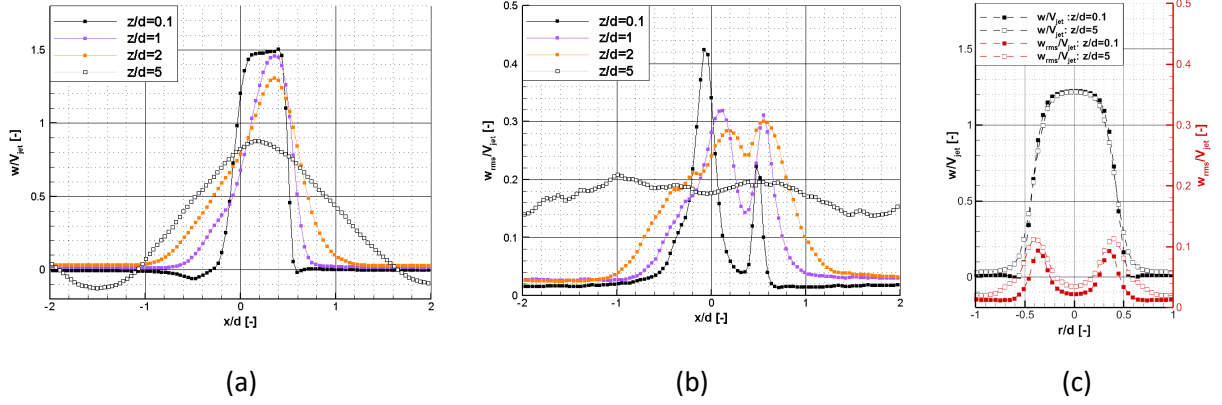


Fig. 9: Velocity profiles from the hole to the plate for a perforated pipe configuration ($Re_j = 5000 - H/d = 7 - VR = 2 - p/d = 3.5$) and a long tube configuration ($Re_j = 5000 - H/d = 7$). (a), (b) Mean and RMS velocities for a perforated pipe: $y/d = 0$ plane, (c) Mean and RMS velocities for a long tube

Once the shear layers merge (at approximately $z/d = 2.5$), mean and RMS velocity profiles homogenize, which leads to more symmetrical jets as they get closer to the impinged plate (Fig. 9 (a)). Finally, close to the impinged plate, a region of negative mean velocity between the stagnation points of each jet (Fig. 7 (c) and Fig. 9 (a) at $z/d = 5$) and **high value of rms velocities** (Fig. 7 (d)) are noticeable. The two zones are located at $x/d = -1.4$ and $x/d = 2.2$ and extend approximately $2d$ far from the impinged plate. This positioning corresponds to the fountain effect resulting from the interaction of the central jet with the previous and subsequent jets. **By contrast, for a fully developed jet, the jet flow in the impinging zone is turned radially along the plate and is not limited by jet interactions. High RMS velocity values are visible close to the plate around $|r/d| = 2.5$ (Fig. 7 (f)), this is due to the interaction of vortices in the shear layer with the impinged plate.**

Fig. 10 shows the Nusselt number distribution for the five central holes. Nusselt number peaks are located at the stagnation point of each jet. The central jet peak of Nusselt number is equal to $Nu_0 = 43.6$ and is located at $x/d = 0.1$, which coincides with the stagnation point observed in velocity fields reported above. Away from the stagnation point, along Y-axis, Nusselt number distribution presents a monotonic decrease trend. Along X-axis, minimum values, $Nu = 30.0$ at $x/d = -1.5$ and $Nu = 27.3$ at $x/d = 2.3$, appear on both sides of the central peak, which corresponds to the positioning of the fountain effect midway between jets.

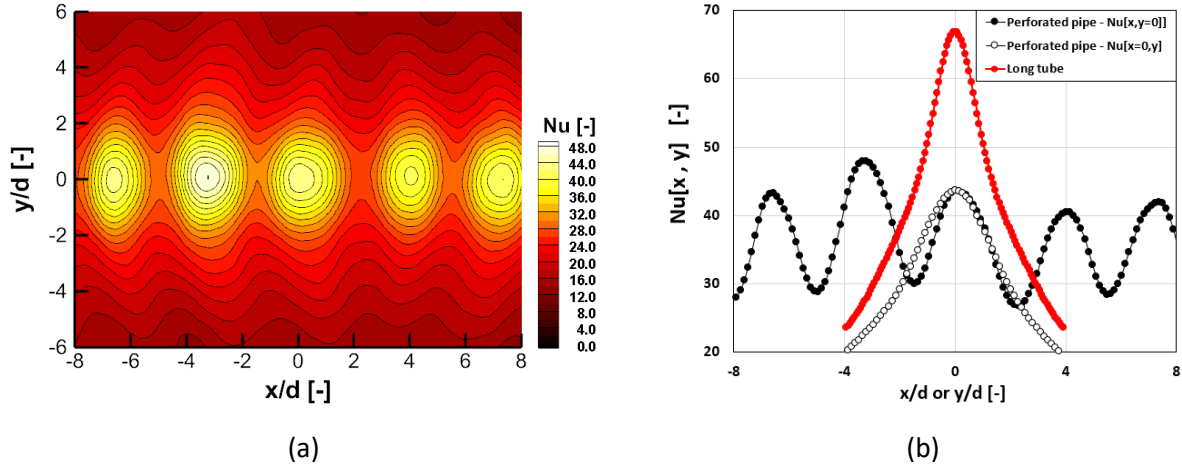


Fig. 10: Nusselt distribution: $Re_j = 5000 - H/d = 7 - VR = 2 - p/d = 3.5$. (a) Nusselt cartography, (b) Nusselt profiles along X-axis and Y-axis

Unlike the results of previous studies on rows of jets without upstream crossflow ([26–28]), there is no visible maximum heat exchange midway between the jets. Associated with the fountain effect, this maximum level is more visible for small injection-to-plate and jet center-to-center distances; in our experiment, these distances are probably overly large. Moreover, previous discussions have shown that compared to more academic and axisymmetric jets, mean and RMS velocity profiles in perforated pipe configuration tend to homogenize significantly after the fusion of shear layers, which may result in smoother interactions midway between the jets and lessened influence of the fountain effect on heat transfer.

Distinct Nusselt number distribution along the streamwise and spanwise directions results in ellipsoidal iso-Nusselt contours at the stagnation points. As seen above, jets emerging from the perforated holes are larger in Y-axis than in X-axis; this may result in a higher heat transfer rate along Y-axis and, consequently, in an ellipsoidal iso-Nusselt contour at the stagnation point.

The Nusselt number at the stagnation point for each jet is not exactly the same as in Fig. 10 (b). The discrepancy can be explained by a slight mass flow rate disparity over the holes or by a jet's disrupting those that follow. To quantify this disparity, the average Nusselt number for each hole (from minimum to minimum Nusselt along X-axis and over $|y/d| = 6$ along Y-axis) have been calculated and compared to the mean Nusselt number along the perforated pipe. Maximum disparity was found for the hole n°3 (approximately 6%) and minimum for the central hole (approximately -0.5%). Jet's outlet mass flow rate was then estimated based on the result that mean Nusselt number varies with a power law dependency

$\overline{Nu} = \alpha Re^{0.6}$ (section 3.4.). Maximum mass flow rate disparity are estimated to be 10-11% (hole n°3) compared to a perfect uniform distribution while the central jet's flow rate disparity is estimated to be less than 1%. This may induce velocity differences between jets. It appears that velocity distributions near the injection ($z/d = 0.1$) are relatively similar for the three central jets as shown in Fig. 7 (a) and (b): normalized maximum mean and rms velocities are 1.5 and 0.4 respectively for the three jets. However, when jets progress from the injection to the impinged plate, velocity distribution between jets becomes less similar (Fig 7. (c)). Jet velocity and Nusselt number discussions are presented for the central jet since mass flow rate disparity (less than 3.5%) and Nusselt number disparities (less than 6%) were minimum for this jet.

Local Nusselt number distribution of a long tube configuration is presented in Fig. 10 (b). At the stagnation point, the Nusselt number is equal to $Nu_0 = 66.9$ and corresponds to an 49% increase compared to the perforated pipe configuration. In the long tube configuration, the impinged plate is located before the end of the potential core, which leads to high mean velocity near the region of the stagnation point ($w/\overline{V}_{jet} = 0.28$ at $z/d = 6.9$, Fig. 7 (e)); while in the perforated pipe configuration, jets have already homogenized when they reach the plate ($w/\overline{V}_{jet} = 0.1$ at $z/d = 6.9$, Fig. 7 (c)). Away from the stagnation point, the Nusselt number along r/d tends to get closer to the local Y-axis distribution of a perforated pipe configuration; $4d$ from the stagnation point, it increases by only 18%. By contrast, the Nusselt number resulting from a fully developed jet decreases steeply away from the stagnation point. **In regards to** the radial velocity profiles, closed to the impinged plate, along $z/d = 6.9$ (not reported here), mean velocity distributions along r/d and y/d become similar $3d$ away from the stagnation point in both configurations. This last point may explain the reason why Nusselt number distributions for the two configurations get closer away from the stagnation point.

Studies conducted in the literature [26] for a row of fully developed jets have been performed for several center-to-center jet values ($p/d > 4$). The influence of multiple interactions between jets has been investigated without upstream crossflow. The authors showed that the interaction is limited to a region midway between jets. They also showed that local Nusselt number distributions are approximately the same compared to those of a single fully developed jet. Consequently, it is likely that heat transfer differences between a perforated pipe and a fully developed jet are due to the upstream crossflow rather than the jets' interactions.

To conclude the discussion about the jet flow structure of perforated pipe and long tube configurations, it is interesting to compare present results to a jet emerging from a perforated plate. The reason being that this latter configuration is between the two tested configurations. For a perforated pipe, some authors (Mi et al. [49]) have shown that the mean velocity profile at the injection hole is flat, by contrast of a parabolic velocity profile observed for a fully developed jet. It is, to some extent, quite similar to the injection mean velocity profile in the effective cross-sectional area of a perforated pipe (section 3.1). The flat mean velocity distribution close to the injection of the jet has a direct effect on the Nusselt number distribution. In particular, Roux et al. [50] have carried out experiments to study the influence of a flat and a parabolic velocity profiles on the Nusselt number distribution. For $Re_j = 28000$, authors have shown that the stagnation Nusselt number decreases by approximately 18% at $H/d = 3$ for a flat velocity profile compared to a parabolic velocity profile. This result is consistent with the discussion above since Nusselt number at stagnation point were also lower for a perforated pipe compared to a long tube (by approximately 49%). As discussed above, the more pronounced decrease might be explain by the upstream crossflow which shortens drastically the potential core.

3.2. Injection-to plate distance parameter effect (H/d)

In this section, the influence of injection-to-plate distance is investigated for $H/d = 3; 5$ and 7 . Effects of this distance on the flow structure have been observed in a fixed configuration ($Re_j = 5000$, $VR = 9.7$ and $p/d = 3.5$), particular features of other injection Reynolds numbers or upstream crossflow will be indicated.

Mean velocity distribution at injection does not depend on the injection-to-plate distance and is identical when the injection Reynolds number and tested VR are set (Fig. 11 (a) and (b)). Consequently, the position of the plate does not affect the mean velocity injection profiles. However, **in regards to** RMS velocity profile along $z/d = 0.1$ (Fig. 11 (c)), turbulence intensity in the region $x/d < -0.5$ is much higher for $H/d = 3$ (8 %) than for $H/d = 5$ and 7 (4 %). For the smallest injection-to-plate distance, the fountain effect occurring between two consecutive jets is close to the injection holes (Fig. 11 (b)); as a result, it interacts directly with the jet at the hole exit. As seen before, the upstream part of the hole is a region where ambient air is sucked into the injection, and which tends to merge with the fountain effect at the lowest injection-to-plate distance $H/d = 3$, resulting in a recirculation zone which extends over $3d$ length along the Z -axis. This zone is presumably coupled with

strong 3D effects and higher turbulence intensity. By contrast, for higher injection-to-plate distances the fountain effect zone does not reach the injection hole exit, and the recirculation zone is no longer visible on the upstream side of the hole (Fig. 11 (a)). It can be deduced that from $H/d > 5$, plate position no longer affects RMS velocity injection profiles. The flow structure described here for configuration $Re_j = 5000$ and $VR = 9.7$ is also visible for lower injection Reynolds numbers $Re_j = 3000$ and 1500 , as well as for lower upstream crossflow intensity $VR = 2$ and 4 .

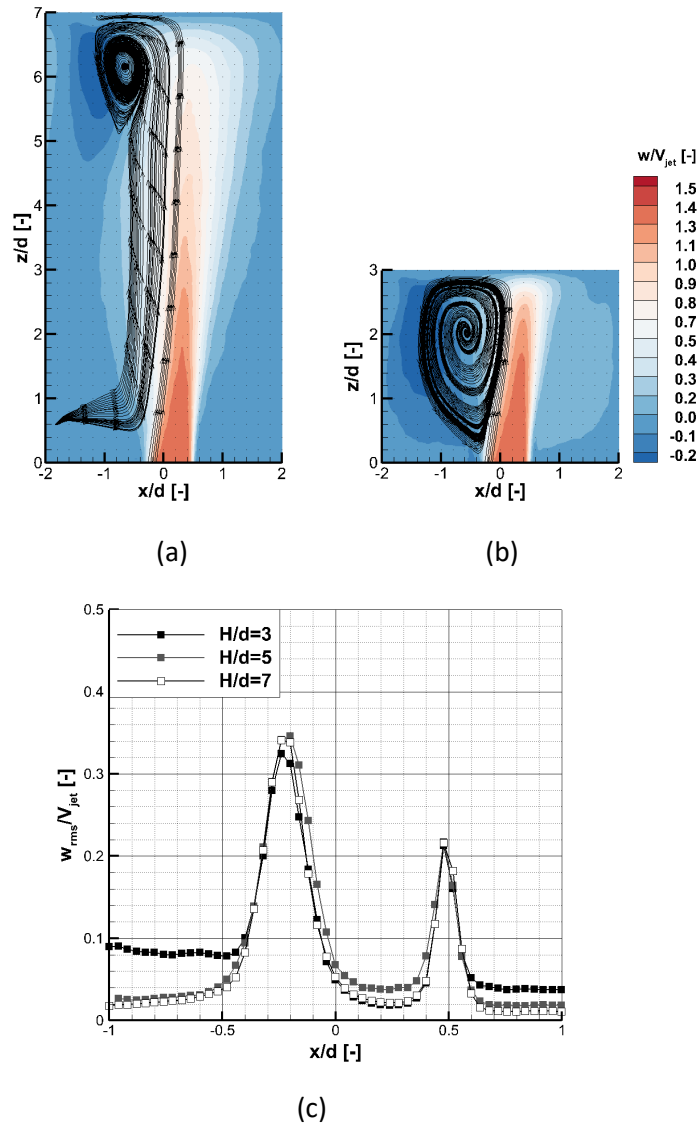


Fig. 11: Effect of H/d on velocity distribution in the plane $y/d = 0$: $Re_j = 5000$ - $VR = 9.7$ - $p/d = 3.5$. (a) $H/d = 7$, (b) $H/d = 3$, (c) Profiles along $z/d=0.1$

In comparison, the influence of H/d on a jet issuing from a long tube is far less complex. As discussed in section 3.1 (Fig. 7 (e) and (f)) for a fully developed jet, the impinging plate is located at the end of the potential core when $H/d = 7$. Consequently, mean

velocity in the center jet region when jet reaches the plate is similar for the three injection-to-plate distance configurations ($3 < H/d < 7$). In regards to turbulence intensity, section 3.1 shows that shear layer tends to grow over the potential core (Fig. 7 (f)). Turbulence intensity values in the shear layer when jet reaches the plate are higher when injection-to-plate distance increases from $H/d = 3$ to $H/d = 7$.

Fig. 12 (a) shows local Nusselt distribution along the streamwise direction. The highest heat transfer rate at stagnation point is obtained for low injection-to-plate distance; when this distance increases, Nusselt number tends to decrease. At the central hole stagnation point and $Re_j = 5000$, Nusselt number goes down from $Nu_0 = 55.6$ for $H/d = 3$ to $Nu_0 = 39.1$ for $H/d = 7$ (30 % decrease). Decreased heat transfer rate at the stagnation point for longer injection-to-plate distances is commonly observed for lower injection Reynolds numbers $Re_j = 3000$ and 1500 (not reported here), and for all VR values tested. In the perforated pipe configuration, even for the smallest distance $H/d = 3$, jets impinge the plate after the end of the potential core; for all injection-to-plate distances, shear layers have already merged and velocity started to decrease when jets reach the plate. In contrast, in the long tube configuration (Fig. 12 (b)), Nusselt number at the stagnation points increases when H/d get larger ($Nu_0 = 61.5$ for $H/d = 3$ versus $Nu_0 = 66.9$ for $H/d = 7$); the jet impinges the plate before the end of the potential core. Mean velocity is then very similar close to the impinged plate for the three injection-to-plate distances, whereas increased turbulence intensity occurs when the jet develops, resulting in a higher heat transfer rate at the stagnation point when H/d increases. For $H/d = 3$, a second maximum is visible at $r/d = 0.3$ and is usually attributed to the interaction of shear layer vortexes with the impinged wall. It disappears progressively for $H/d = 5$ and then completely for $H/d = 7$. For semi-turbulent jet $Re_j = 3000$, Nusselt at the stagnation point is identical for the three injection-to-plate distances ($Nu_0 = 51.1$). As seen above in Kuang et al. [21]'s study, overall heat transfer remains almost unchanged, the reason being that the impinged plate is located inside the undisturbed region of the jet.

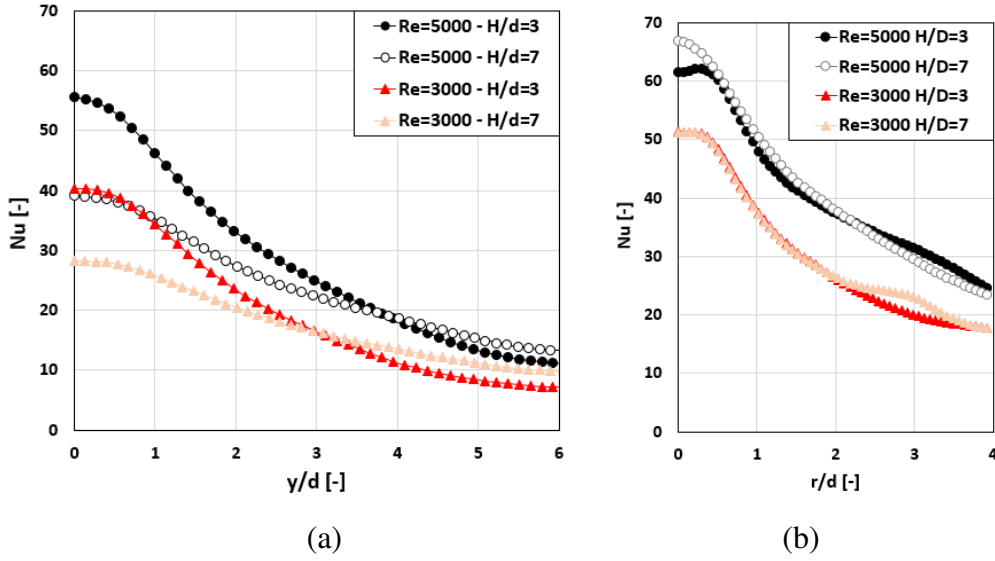


Fig. 12: Effect of H/d on Nusselt distribution for perforated pipe ($VR = 9.7 - p/d = 3.5$) and long tube configurations. (a) Perforated pipe (central hole): local Y-axis profile, (b) Long tube: radial profile

Nusselt number distribution in the streamwise direction decreases more sharply for lower injection-to-plate distances (Fig. 12 (a)), and the local Nusselt number far from the stagnation point consequently becomes greater for large injection-to-plate distances. For $Re_j = 5000$, local Nusselt number is equal to 18.3 at $y/d = 4$ for $H/d = 3$ versus $Nu = 18.6$ for $H/d = 7$. In addition, mean velocity profiles along Y-axis measured $0.1d$ away from the impinging plate for $H/d = 3$ and 7 (not reported here) show that mean velocity decreases more sharply for $H/d = 3$: this is possibly due strong 3D effects caused by the prominent recirculation zone, which may induce a different flow distribution close to the impinging plate than in a classical wall jet region. The decreased Nusselt profile along Y-axis is even more pronounced when the injection Reynolds number is low.

Considering mean heat transfer rate, Nusselt number distribution was averaged along X-axis over the five central holes and along Y-axis over $y/d = \pm 6$, results showed an optimum heat transfer rate at the injection-to-plate distance $H/d = 5$ for both configurations $Re_j = 3000$ and 1500 . It corresponds to the lowest injection-to-plate distance at which the rise of Nusselt number at the stagnation point no longer compensates for the decrease of heat transfer along the streamwise direction. In contrast to long tube configurations (Gardon and Akfirat [12]), the position of this optimum is not related to the length of the potential core but rather, in all likelihood, to the interaction between jets, in which case the position also depends on jet-to-jet spacing (section 3.5).

3.3. Upstream crossflow parameter effect (VR)

The effect of the velocity ratio $VR = \overline{V}_{jet} / \overline{V}_{pipe}$ has been investigated from 2 to 9.7 for a fixed perforated pipe configuration: $Re_j = 5000$, $H/d = 7$ and $p/d = 3.5$. VR parameter characterizes the intensity of upstream crossflow within the pipe, which is strong for low VR , while $VR = 9.7$ when all mass flow rate fed within the pipe exits through the injection holes (the valve at the pipe exit is closed).

Fig. 13 (a) shows the effect of VR on mean velocity profiles near the injection hole along $z/d = 0.1$ and in the plane $y/d = 0$. With high upstream crossflow $VR = 2$, as seen in section 3.1, jets tend to emerge only from the downstream part of the injection hole (from $x/d = 0.1$ to $x/d = 0.4$) When the crossflow in the pipe decreases (higher VR value), the effective cross-sectional area increases; the plate region with maximum mean velocity is enlarged between $x/d = -0.1$ and $x/d = 0.4$ for $VR = 9.7$, which results in a decrease of the maximum mean velocity to $w / \overline{V}_{jet} = 1.3$. And for low upstream crossflow, centrifugal force is lower when the main flow in the pipe curves. As a result, separation between the flow within the pipe and the jet through the injection hole is located close to the upstream lip of the hole. This is further confirmed by the reduction of the region of ambient air sucked into the hole; negative mean velocity is noticeable from $x/d = -0.5$ to $x/d = -0.3$ for $VR = 2$ and is reduced in the region between $x/d = -0.5$ and $x/d = -0.4$ for $VR = 9.7$. When the crossflow in the pipe decreases, the mean velocity profile at injection tends to resemble jet issuing from a long tube, which indicates that the influence of the crossflow supply has become limited. **In regards to** the velocity profiles along $z/d = 0.1$ for the six planes detailed in Fig. 3, the effective cross-sectional area is estimated at between 60% and 70% of the total hole area for $VR = 2$ with a prominent crescent shape, and between 75% and 80% of the total hole area for $VR = 9.7$, with a scarcely visible crescent shape.

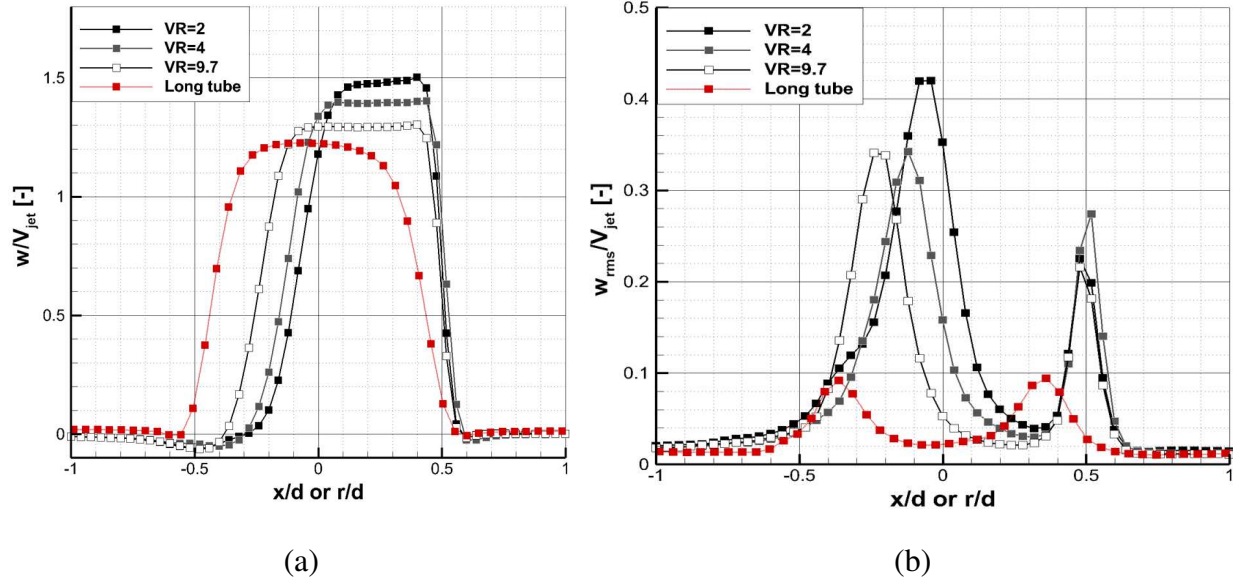


Fig. 13: Effect of VR on velocity profiles at $z/d = 0.1$ in the plane $y/d = 0$: $Re_j = 5000 - H/d=7$. (a) Mean velocity (b) RMS velocity

The increase of the cross-section area when VR decreases tends to enlarge the potential core and then to shift the shear layer position. As seen in Fig. 13 (b), the upstream peak located at $x/d = -0.05$ for $VR = 2$ moves to $x/d = -0.25$. At this point, shear layer moves towards the upstream lip of the hole since the region of ambient air sucked in the hole is reduced for lower upstream crossflow. Moreover, the turbulent intensity generated in the shear layer decreases from 42% for $VR = 2$ down to 34% for $VR = 9.7$; as mentioned, centrifugal force is lower when the main flow in the pipe curves, which may result in lower turbulence intensity in the shear layer. In contrast, peak RMS velocity in the downstream lip of the hole does not change ($x/d = 0.45$) for all VR values and maintains about the same intensity (24%). In this zone, the shear layer is triggered by the downstream lip of the hole rather than the crossflow, resulting in limited effect of VR parameters on turbulence intensity. In this range of VR values, turbulence intensity in the shear layer of perforated pipe configuration is much higher than in a long tube configuration. This may indicate that the maximum VR tested, $VR = 9.7$, does not suffice to characterize cases where the influence of upstream crossflow is negligible.

For high upstream crossflow ($VR = 2$), Fig 14 shows that the jet emerges from the downstream half of the hole and is then deviated from higher to lower x value when it grows. For $VR = 9.7$ (lower upstream crossflow), the deviation is not as pronounced (Fig 14 (b)). It results that the central jet stagnation point moves from $x/d \approx 0.5$ for $VR = 9.7$ to $x/d \approx 0.1$ for $VR = 2$. Location of the fountain effect shifts similarly.

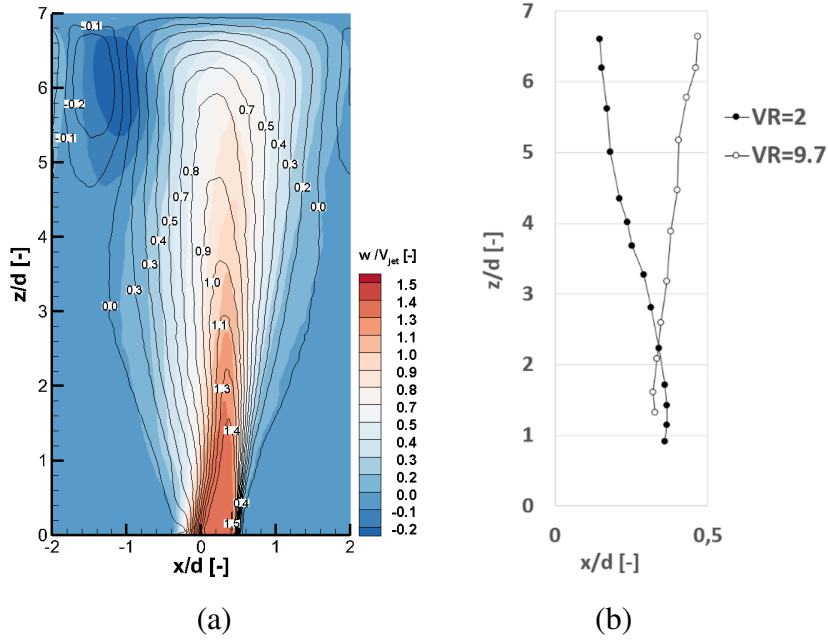


Fig. 14: Effect of VR on the jet flow structure: (a) Mean velocity fields for $VR = 2$ (lines) and $VR = 9.7$ (flood), (b) position of the maximum mean velocity

Fig. 15 shows local Nusselt number in the streamwise and the spanwise directions for $VR = 2$ and $VR = 9.7$. The Nusselt number is locally higher for high upstream crossflow. In the central jet, Nu at stagnation point is reduced from 43.5 at $x/d = 0$ for $VR = 2$ to 38.8 at $x/d = 0.5$ for $VR = 9.7$. The mean Nusselt number, \overline{Nu}_{6d} , averaged along X-axis over the central hole and along Y-axis over $y/d = \pm 6$, is reduced by 9.4% from $VR = 2$ to $VR = 9.7$. The reduction of \overline{Nu}_{6d} is equal to 3.8% for $H/d = 5$ and to 0.6% for $H/d = 3$. The effect of VR on the Nusselt number intensity is small, this can be explained by the fact that the impinging plate is located far from the shear layer fusion. As seen previously, the mean and RMS velocity profiles tend to homogenize once shear layers merge. The influence of the upstream crossflow condition becomes then limited, which **results in low dependency of heat transfer rate on VR** , which is shown here for injection-to-plate distance equal to $H/d = 7$, and it is also visible at lower distances $H/d = 5$ and $H/d = 3$. Furthermore, the position of the maximum Nusselt number observed at $x/d = 0.1$ for $VR = 2$ and $x/d = 0.5$ for $VR = 9.7$ corresponds to the location of the stagnation point of the central jet measured using the PIV method (Fig. 4). In point of fact, the shift of the maximum Nusselt number toward negative x value results from the deviation of the jets in this direction, when they approach the impinging plate.

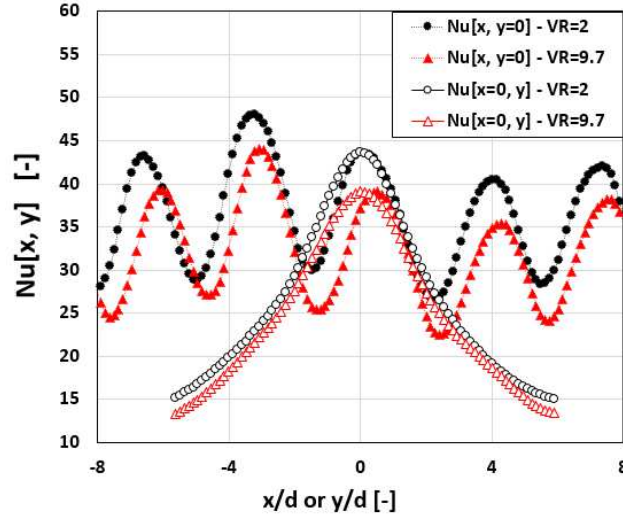


Fig. 15: Effect of VR on local Nusselt distribution: $Re_j = 5000 - H/d = 7$

3.4. Injection Reynolds parameter effect (Re_j)

In this section, the influence of the injection Reynolds number is investigated for three injection Reynolds numbers, $Re_j = 1500$; 3000 and 5000, corresponding to a laminar, a semi-turbulent and a fully turbulent flow respectively, in Mcnaughton and Sinclair [17]'s classification. As above, effects of the injection Reynolds on the flow structure are observed for a fixed configuration ($H/d = 5$, $VR = 9.7$ and $p/d = 3.5$), and the particular features of other injection-to-plate distances or upstream crossflow are specified, if necessary.

Jet flow structures issuing from perforated pipes are quite similar, whatever injection the Reynolds numbers tested; that is why they are not reported here. The conclusions drawn in the previous section for $Re_j = 5000$ (reduced cross-sectional area, highly asymmetrical and 3D aspect of jets, homogenization of velocity profiles close to the impinged plate...) also apply to injection Reynolds numbers equal to 3000 and 1500. A slight increase of the normalized maximum mean velocity remains noticeable for lower injection Reynolds numbers at the exit holes $z/d = 0.1$; w/\overline{V}_{jet} increases from 1.3 for $Re_j = 5000$ (Fig. 16 (a)) up to 1.4 for $Re = 3000$. This trend is also visible in the long tube configuration (Fig. 16 (b)): w/\overline{V}_{jet} increases from 1.2 for $Re_j = 5000$ up to 1.3 for $Re_j = 3000$. This is consistent with the result that the ratio of maximum to average velocity profile is parabolic for laminar or semi-turbulent flow and more flattened for turbulent flow.

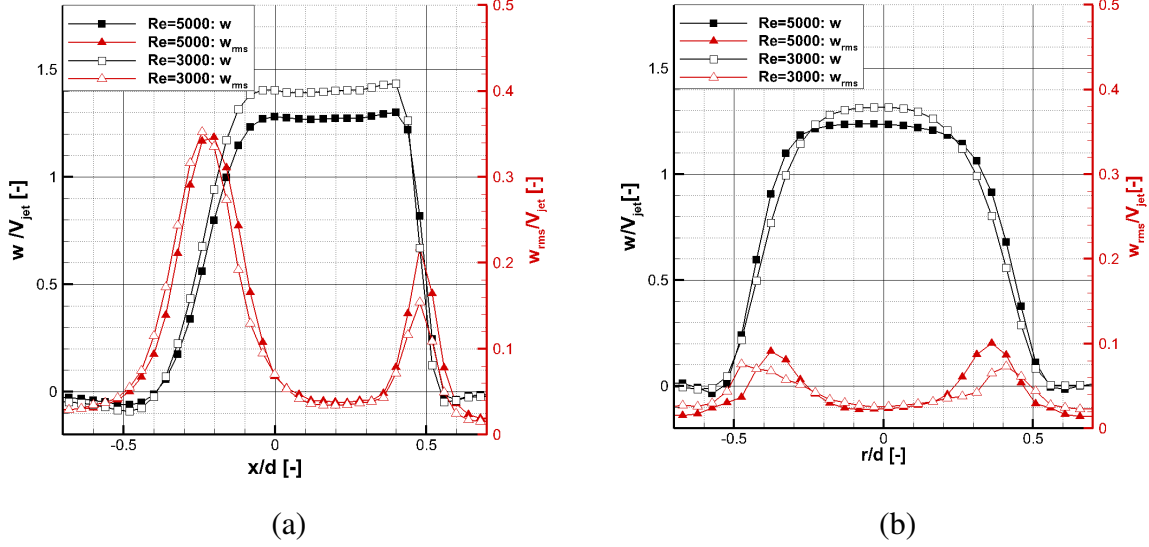


Fig. 16: Effect of Re_j on velocity profiles along $z/d = 0.1$: $H/d = 5$ - $VR = 9.7$ - $p/d = 3.5$. (a) Perforated pipe: plane $y/d = 0$, (b) Long tube

In regards to RMS velocity (Fig. 16 (a)), normalized RMS velocities are predictably lower for lower Reynolds number. As seen previously, the shear layer is most likely generated due to the sudden deviation of the crossflow within the pipe for the upstream region of the hole and to the lip of the hole in the downstream region; these two effects have a smaller role for lower injection Reynolds numbers, and probably lead to lower turbulent intensity in the shear layer. Since crossflow within the pipe remains identical ($VR = 9.7$), the positions of the two peaks of RMS velocity ($x/d = -0.25$ and $x/d = 0.45$) are identical for all the Reynolds numbers tested.

The influence of injection Reynolds number on heat transfer was also studied between $Re_j = 1500$ and 5000 and for $VR = 9.7$. Nusselt number was shown to vary with power law dependency $Nu \propto Re_j^n$. More specifically, trend dependency was investigated for the average Nusselt \overline{Nu}_{6d} : $n = 0.59$ for $H/d = 7$. The n value then tends to increase for lower injection-to-plate distances: $n = 0.64$ for $H/d = 5$ and $n = 0.76$ for $H/d = 3$.

3.5. Pitch parameter effect (p/d)

The influence of jet-to-jet spacing on a perforated pipe configuration is investigated from $p/d = 2.25$ to $p/d = 5.8$ for different injection-to-plate distances at $Re_j = 5000$ and $VR = 9.7$.

Fig. 17 presents the effect of p/d on local Nusselt distribution along the streamwise and the spanwise directions. Whatever the H/d , the Nusselt value at the stagnation point for the three jet-to-jet center distances is quite similar. Along X-axis (Fig. 17 (a)), Nusselt number

distribution is nearly the same for the three p/d values in the vicinity of the stagnation point ($|x|/d < 1$). By contrast, Nusselt number distribution differs in the jet encounter regions (around $|x|/d = 1$ for $p/d = 2.25$ and $|x|/d = 1.6$ for $p/d = 3.5$). The influence of adjacent jets seems limited to a region located midway between jets, a hypothesis corroborated in Fig. 17 (b); the Nusselt profiles along Y-axis are identical, a finding indicating low dependency of p/d along Y-axis.

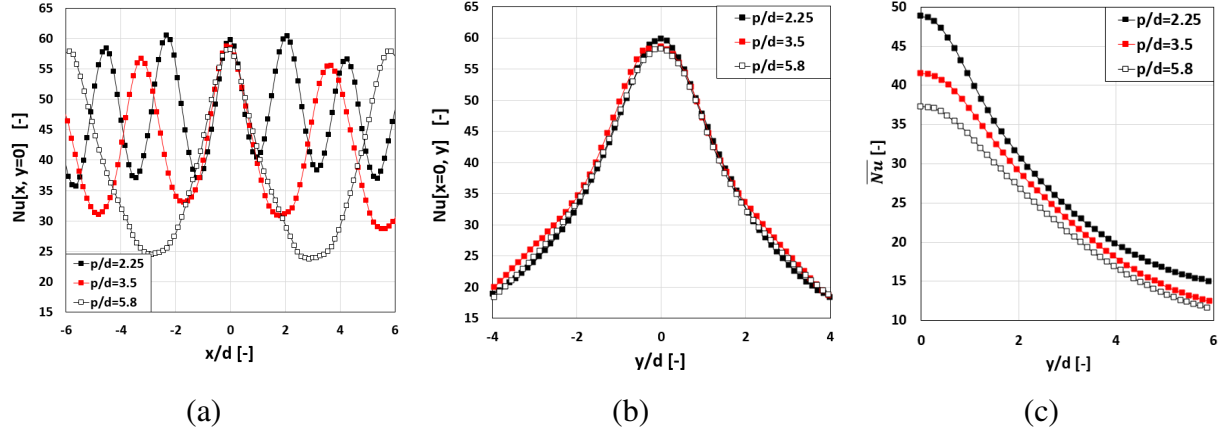


Fig. 17: Effect of p/d on Nusselt distribution: $Re_j = 5000$ - $VR = 9.7$ - $H/d = 3$. (a) Along X-axis, (b) Along Y-axis, (c) Averaged Nusselt distribution

To complement the local analysis, Nusselt number distribution along X direction was integrated at a fixed y/d . The line averaged Nusselt number distribution, $\overline{Nu}(y/d)$, is presented in Fig. 17 (c). For a fixed injection Reynolds and injection-to-plate distance, the averaged Nusselt number is higher for low jet-to-jet spacing. In point of fact, the coolant flow per unit area of impinged surface is larger for $p/d = 2.25$ compared to $p/d = 3.5$ and $p/d = 5.8$, the reason being that the jets are closer to each other. As seen above, reduction of center-to-center jet spacing not only increases the local Nusselt number midway between the jets, but also induces a significant increase of the mass flow rate. Hence, the influence of jet-to-jet spacing has been investigated for a fixed coolant flow per unit area rather than a fixed injection Reynolds number. The average Nusselt number \overline{Nu}_{6d} calculated over $y/d = \pm 6d$ (not presented here) is demonstrably higher for a larger jet-to-jet distance at a fixed coolant flow per unit area.

Results are reported here for fixed $VR = 9.7$ and $Re_j = 5000$, and trends remain identical for lower VR and Re_j . More specifically, heat transfer rates for all p/d values varies only slightly when VR decreases (as seen for the $p/d = 3.5$ configuration in section 3.3). The conclusions drawn in the previous sections for $p/d = 3.5$ on the influence of injection

Reynolds ($\overline{Nu}_{6d} \propto Re_j^n$) and on the effects of H/d (pronounced decrease of heat transfer rate near the stagnation point when H/d increases and low dependency for larger y/d) also apply to other p/d values.

Conclusion

An experimental investigation was carried out to determine the flow and heat transfer characteristics of a row of jets issuing from the holes of a perforated pipe. The influence of H/d , Re_j , VR , p/d were studied and resulted on the following conclusions:

- Jets emerging from perforated pipe tend to emerge with an effective cross-sectional area reduced to a crescent shape. The dissymmetry of the jet persists until approximately $z/d = 3$ and disappears progressively once shear layers merge.
- Heat transfer resulting from a perforated pipe configuration shows ellipsoidal iso-Nusselt contours at the stagnation points with relatively low values compared to a fully developed jet.
- The highest Nusselt number at stagnation point is obtained for low injection-to-plate distance $H/d = 3$. However, an optimum mean Nusselt number can be seen for higher H/d depending on Re_j and p/d .
- Mean Nusselt numbers were shown to vary with a power law dependency $Nu_{6d} \propto Re_j^n$ ($0.6 < n < 0.7$), similarly to a fully developed jet.
- The influence of VR becomes very limited once the shear layers merge close to the impinging plate, resulting in a relatively low influence of VR on heat transfer.
- For a fixed Re_j , the mean Nusselt number is higher for small p/d . However, it was shown that setting the coolant flow per unit area rather than Re_j leads to a higher mean heat transfer rate for more elevated p/d values.

Acknowledgements

The English-language text has been reviewed and edited by an American translator, Jeffrey Arsham, whom we thank for his contribution.

- [1] R. Viskanta, Heat transfer to impinging isothermal gas and flame jets, *Exp. Therm. Fluid Sci.* 6 (1993) 111–134. [https://doi.org/10.1016/0894-1777\(93\)90022-B](https://doi.org/10.1016/0894-1777(93)90022-B).
- [2] N. Zuckerman, N. Lior, Impingement Heat Transfer: Correlations and Numerical Modeling, *J. Heat Transf.* 127 (2005) 544–552. <https://doi.org/10.1115/1.1861921>.

- [3] H. Martin, Heat and Mass Transfer between Impinging Gas Jets and Solid Surfaces, in: J.P. Hartnett, T.F. Irvine (Eds.), *Adv. Heat Transf.*, Elsevier, 1977: pp. 1–60. [https://doi.org/10.1016/S0065-2717\(08\)70221-1](https://doi.org/10.1016/S0065-2717(08)70221-1).
- [4] G.M. Carlomagno, A. Ianiro, Thermo-fluid-dynamics of submerged jets impinging at short nozzle-to-plate distance: A review, *Exp. Therm. Fluid Sci.* 58 (2014) 15–35. <https://doi.org/10.1016/j.expthermflusci.2014.06.010>.
- [5] J.W. Gauntner, P. Hrycak, J.N.B. Livingood, Survey of literature on flow characteristics of single turbulent jet impinging on flat plate, 1970. <https://ntrs.nasa.gov/citations/19700009658> (accessed September 18, 2020).
- [6] H. Fellouah, C.G. Ball, A. Pollard, Reynolds number effects within the development region of a turbulent round free jet, *Int. J. Heat Mass Transf.* 52 (2009) 3943–3954. <https://doi.org/10.1016/j.ijheatmasstransfer.2009.03.029>.
- [7] S. Ashforth-Frost, K. Jambunathan, Effect of nozzle geometry and semi-confinement on the potential core of a turbulent axisymmetric free jet, *Int. Commun. Heat Mass Transf.* 23 (1996) 155–162. [https://doi.org/10.1016/0735-1933\(96\)00001-2](https://doi.org/10.1016/0735-1933(96)00001-2).
- [8] D. Lytle, B.W. Webb, Air jet impingement heat transfer at low nozzle-plate spacings, *Int. J. Heat Mass Transf.* 37 (1994) 1687–1697. [https://doi.org/10.1016/0017-9310\(94\)90059-0](https://doi.org/10.1016/0017-9310(94)90059-0).
- [9] V.V. Katti, S.N. Yaraswy, S.V. Prabhu, Local heat transfer distribution between smooth flat surface and impinging air jet from a circular nozzle at low Reynolds numbers, *Heat Mass Transf.* 47 (2011) 237–244. <https://doi.org/10.1007/s00231-010-0716-1>.
- [10] J. Lee, S.-J. Lee, The effect of nozzle configuration on stagnation region heat transfer enhancement of axisymmetric jet impingement, *Int. J. Heat Mass Transf.* 43 (2000) 3497–3509. [https://doi.org/10.1016/S0017-9310\(99\)00349-X](https://doi.org/10.1016/S0017-9310(99)00349-X).
- [11] P. Gulati, V. Katti, S.V. Prabhu, Influence of the shape of the nozzle on local heat transfer distribution between smooth flat surface and impinging air jet, *Int. J. Therm. Sci.* 48 (2009) 602–617. <https://doi.org/10.1016/j.ijthermalsci.2008.05.002>.
- [12] R. Gardon, J.C. Akfirat, Heat Transfer Characteristics of Impinging Two-Dimensional Air Jets, *J. Heat Transf.* 88 (1966) 101–107. <https://doi.org/10.1115/1.3691449>.
- [13] K. Kataoka, M. Suguro, H. Degawa, K. Maruo, I. Mihata, The effect of surface renewal due to largescale eddies on jet impingement heat transfer, *Int. J. Heat Mass Transf.* 30 (1987) 559–567. [https://doi.org/10.1016/0017-9310\(87\)90270-5](https://doi.org/10.1016/0017-9310(87)90270-5).
- [14] J.W. Baughn, S. Shimizu, Heat Transfer Measurements From a Surface With Uniform Heat Flux and an Impinging Jet, *J. Heat Transf.* 111 (1989) 1096–1098. <https://doi.org/10.1115/1.3250776>.
- [15] M. Hadžiabdić, K. Hanjalić, Vortical structures and heat transfer in a round impinging jet, *J. Fluid Mech.* 596 (2008) 221–260. <https://doi.org/10.1017/S002211200700955X>.
- [16] T.S. O’Donovan, D.B. Murray, Jet impingement heat transfer – Part II: A temporal investigation of heat transfer and local fluid velocities, *Int. J. Heat Mass Transf.* 50 (2007) 3302–3314. <https://doi.org/10.1016/j.ijheatmasstransfer.2007.01.047>.
- [17] K.J. Mcnaughton, C.G. Sinclair, Submerged jets in short cylindrical flow vessels, *J. Fluid Mech.* 25 (1966) 367–375. <https://doi.org/10.1017/S0022112066001708>.
- [18] D. Violato, A. Ianiro, G. Cardone, F. Scarano, Three-dimensional vortex dynamics and convective heat transfer in circular and chevron impinging jets, *Int. J. Heat Fluid Flow.* 37 (2012) 22–36. <https://doi.org/10.1016/j.ijheatfluidflow.2012.06.003>.
- [19] R. Vinze, S. Chandel, M.D. Limaye, S.V. Prabhu, Influence of jet temperature and nozzle shape on the heat transfer distribution between a smooth plate and impinging air jets, *Int. J. Therm. Sci.* 99 (2016) 136–151. <https://doi.org/10.1016/j.ijthermalsci.2015.08.009>.
- [20] M. Angioletti, R.M. Di Tommaso, E. Nino, G. Ruocco, Simultaneous visualization of flow field and evaluation of local heat transfer by transitional impinging jets, *Int. J. Heat Mass Transf.* 46 (2003) 1703–1713. [https://doi.org/10.1016/S0017-9310\(02\)00479-9](https://doi.org/10.1016/S0017-9310(02)00479-9).
- [21] J.J. Kuang, X.L. Wang, T.J. Lu, T. Kim, Role of Laminar Length of Round Jet Impinging on Metal Foams, *J. Thermophys. Heat Transf.* 30 (2016) 103–110. <https://doi.org/10.2514/1.T4567>.

- [22] W. Rohlf, H.D. Haustein, O. Garbrecht, R. Kneer, Insights into the local heat transfer of a submerged impinging jet: Influence of local flow acceleration and vortex-wall interaction, *Int. J. Heat Mass Transf.* 55 (2012) 7728–7736. <https://doi.org/10.1016/j.ijheatmasstransfer.2012.07.081>.
- [23] C. Carcasci, An experimental investigation on air impinging jets using visualisation methods, *Int. J. Therm. Sci.* 38 (1999) 808–818. [https://doi.org/10.1016/S1290-0729\(99\)80036-2](https://doi.org/10.1016/S1290-0729(99)80036-2).
- [24] W. Wright, An Evaluation of Jet Impingement Heat Transfer Correlations for Piccolo Tube Application, in: 2004. <https://doi.org/10.2514/6.2004-62>.
- [25] R.J. Goldstein, W.S. Seol, Heat transfer to a row of impinging circular air jets including the effect of entrainment, *Int. J. Heat Mass Transf.* 34 (1991) 2133–2147. [https://doi.org/10.1016/0017-9310\(91\)90223-2](https://doi.org/10.1016/0017-9310(91)90223-2).
- [26] M. Fénot, J.-J. Vullierme, E. Dorignac, Local heat transfer due to several configurations of circular air jets impinging on a flat plate with and without semi-confinement, *Int. J. Therm. Sci.* 44 (2005) 665–675. <https://doi.org/10.1016/j.ijthermalsci.2004.12.002>.
- [27] X. Yan, N. Saniei, Measurements of Local Heat Transfer Coefficients from a Flat Plate to a Pair of Circular Air Impinging Jets, *Exp. Heat Transf.* 9 (1996) 29–47. <https://doi.org/10.1080/08916159608946512>.
- [28] N. Koopman, E.M. Sparrow, Local and average transfer coefficients due to an impinging row of jets, *Int. J. Heat Mass Transf.* 19 (1976) 673–683. [https://doi.org/10.1016/0017-9310\(76\)90051-X](https://doi.org/10.1016/0017-9310(76)90051-X).
- [29] A.M. Huber, R. Viskanta, Effect of jet-jet spacing on convective heat transfer to confined, impinging arrays of axisymmetric air jets, *Int. J. Heat Mass Transf.* 37 (1994) 2859–2869. [https://doi.org/10.1016/0017-9310\(94\)90340-9](https://doi.org/10.1016/0017-9310(94)90340-9).
- [30] B.R. Hollworth, R.D. Berry, Heat Transfer From Arrays of Impinging Jets with Large Jet-to-Jet Spacing, *J. Heat Transf.* 100 (1978) 352–357. <https://doi.org/10.1115/1.3450808>.
- [31] S. Pachpute, B. Premachandran, Turbulent multi-jet impingement cooling of a heated circular cylinder, *Int. J. Therm. Sci.* 148 (2020) 106167. <https://doi.org/10.1016/j.ijthermalsci.2019.106167>.
- [32] R. Da Soghe, B. Facchini, M. Micio, D. Coutandin, Heat Transfer and Pressure Drop Analysis of a Turbine Casing Impingement Cooling System, in: American Society of Mechanical Engineers Digital Collection, 2013: pp. 301–310. <https://doi.org/10.1115/GT2012-68793>.
- [33] N. Hay, D. Lampard, Discharge Coefficient of Turbine Cooling Holes: A Review, *J. Turbomach.* 120 (1998) 314–319. <https://doi.org/10.1115/1.2841408>.
- [34] R. Da Soghe, B. Facchini, M. Micio, A. Andreini, Aerothermal Analysis of a Turbine Casing Impingement Cooling System, *Int. J. Rotating Mach.* 2012 (2012) e103583. <https://doi.org/10.1155/2012/103583>.
- [35] K. Marzec, A. Kucaba-Pietal, Numerical investigation of a heat transfer characteristics of an impingement cooling system with non-uniform temperature on a cooled surface, 745 (2016) 032071. <https://doi.org/10.1088/1742-6596/745/3/032071>.
- [36] F. Ben Ahmed, R. Tucholke, B. Weigand, K. Meier, Numerical Investigation of Heat Transfer and Pressure Drop Characteristics for Different Hole Geometries of a Turbine Casing Impingement Cooling System, in: American Society of Mechanical Engineers Digital Collection, 2012: pp. 1095–1108. <https://doi.org/10.1115/GT2011-45251>.
- [37] M. Imbriale, A. Ianiro, C. Meola, G. Cardone, Convective heat transfer by a row of jets impinging on a concave surface, *Int. J. Therm. Sci.* 75 (2014) 153–163. <https://doi.org/10.1016/j.ijthermalsci.2013.07.017>.
- [38] M. Fénot, E. Dorignac, Heat transfer and flow structure of an impinging jet with upstream flow, *Int. J. Therm. Sci.* 109 (2016) 386–400. <https://doi.org/10.1016/j.ijthermalsci.2016.06.010>.
- [39] M. Soleimani nia, B. Maxwell, P. Oshkai, N. Djilali, Measurements of flow velocity and scalar concentration in turbulent multi-component jets: asymmetry and buoyancy effects, *Exp. Fluids.* 61 (2020) 76. <https://doi.org/10.1007/s00348-020-2902-3>.

- [40] D.R. Neal, A. Sciacchitano, B.L. Smith, F. Scarano, Collaborative framework for PIV uncertainty quantification: the experimental database, *Meas. Sci. Technol.* 26 (2015) 074003. <https://doi.org/10.1088/0957-0233/26/7/074003>.
- [41] A. Sciacchitano, D.R. Neal, B.L. Smith, S.O. Warner, P.P. Vlachos, B. Wieneke, F. Scarano, Collaborative framework for PIV uncertainty quantification: comparative assessment of methods, *Meas. Sci. Technol.* 26 (2015) 074004. <https://doi.org/10.1088/0957-0233/26/7/074004>.
- [42] B. Wieneke, PIV uncertainty quantification from correlation statistics, *Meas. Sci. Technol.* 26 (2015) 074002. <https://doi.org/10.1088/0957-0233/26/7/074002>.
- [43] A. Sciacchitano, B. Wieneke, PIV uncertainty propagation, *Meas. Sci. Technol.* 27 (2016) 084006. <https://doi.org/10.1088/0957-0233/27/8/084006>.
- [44] M. Fénot, X.T. Trinh, E. Dorignac, Flow and heat transfer of a compressible impinging jet, *Int. J. Therm. Sci.* 136 (2019) 357–369. <https://doi.org/10.1016/j.ijthermalsci.2018.10.035>.
- [45] B. Giachetti, M. Fénot, D. Couton, F. Plourde, Influence of Reynolds number synthetic jet dynamic in crossflow configuration on heat transfer enhancement, *Int. J. Heat Mass Transf.* 118 (2018) 1–13. <https://doi.org/10.1016/j.ijheatmasstransfer.2017.10.097>.
- [46] C. Robert, G. Casella, *Monte Carlo Statistical Methods*, 2nd ed., Springer-Verlag, New York, 2004. <https://doi.org/10.1007/978-1-4757-4145-2>.
- [47] M. Fénot, Heat transfer and flow structure of a hot annular impinging jet, *Int. J. Therm. Sci.* (2021) 13.
- [48] S.-J.L. Jungho Lee, STAGNATION REGION HEAT TRANSFER OF A TURBULENT AXISYMMETRIC JET IMPINGEMENT, *Exp. Heat Transf.* (2010). <https://doi.org/10.1080/089161599269753>.
- [49] J. Mi, G.J. Nathan, D.S. Nobes, Mixing Characteristics of Axisymmetric Free Jets From a Contoured Nozzle, an Orifice Plate and a Pipe, *J. Fluids Eng.* 123 (2001) 878–883. <https://doi.org/10.1115/1.1412460>.
- [50] S. Roux, M. Fénot, G. Lalizel, L.-E. Brizzi, E. Dorignac, Experimental investigation of the flow and heat transfer of an impinging jet under acoustic excitation, *Int. J. Heat Mass Transf.* 54 (2011) 3277–3290. <https://doi.org/10.1016/j.ijheatmasstransfer.2011.03.059>.